

Politecnico di Torino

Department of Environment,

Land and Infrastructure Engineering

Master of Science in Georesources and Geoenergy Engineering

Evaluation of geophysical and mechanical rock properties through analysis of public well logs in Central-Eastern Italy and the Adriatic Offshore and case study of CO₂ storage potential.

Candidate:

Stybayev Dinmukhamed

Supervisor:

Prof. Christoforos Benetatos

Abstract

The interpretation of geophysical and mechanical rock properties is essential for subsurface characterization, reservoir modeling and future development. This work focuses on the Central-Eastern Italy and Adriatic offshore areas, exploiting a publicly available well log database.

Sonic logs (DT logs) were digitized and processed using Schlumberger Petrel software (v2013) to derive compressional-wave velocity (V_p) and shear-wave velocity (V_s) through empirical equations. The geophysical properties together with a derived density log were used for Dynamic Elastic Moduli (Young's Modulus) calculation for the above region.

A preliminary stratigraphic analysis was performed to investigate relations between lithology and geophysical and mechanical parameters. During the log analysis a potential interval suitable for CO₂ storage was selected for which was performed a preliminary storage capacity calculation.

The results show consistent correlations between seismic velocities and mechanical parameters. These findings can be used for the prediction of mechanical properties in wells with missing data and used during the construction and population of geomechanical models, providing the basis for future subsurface evaluations in the area.

Table of contents

	Abstract	2
1.	Introduction	6
á	a. Geology of the area	6
l	b. Scope of work	8
2.	Data used	9
á	a. Wells	9
ŀ	b. Well logs	10
(c. Digitalization process	12
(d. Use of empirical relations	15
3.	Model construction	26
á	a. Description of the model	26
l	b. Different methods used for value distributing	29
(c. Results	31
4.	CO ₂ case study	34
Co	onclusion	42
D ₀	forances	13

List of figures

Figure 1.1 : Geological sketch of UMAF (Conti, et al., 2020). The geologic units we grouped into 11 rock categories according to their lithology and stratigraphical positions.	
Dotted black line limits the high Ksn value area.	
Figure 1.2: Inferred drainage directions, drainage areas and sediment discharge	
(Maselli, et al. 2011)	7
Figure 2.1 : Study area in the northern Marche (Italy): costal line from Pesaro and Urbino to San Benedetto del Tronto with adjoining mid-Adriatic shelf. Green symbolindicate wells used in this study; the grey polygon outlines the analysis domain (God Earth)	ols ogle 9
Figure 2.2: Carmela 001 and Vasari 001 DIR (from left to right)	
Figure 2.3: Steps of digitalization (section from Carmela 001)	
Figure 2.4 : The photo-scanned log (left) was digitized (right) by Petrel 2013 (Carmo	
001)	
Figure 2.5: The DT (μs/ft) histogram of digitalized log (Petrel 2013)	
Figure 2.6 : The DT (μ s/ft) Histogram of 13 wells in study area (Petrel 2013)	
Figure 2.7: Laboratory V _p -V _s data for water saturated sandstone (Mavko, et al., 200	
Figure 2.8 : Laboratory V _p -density data for sandstone (Mavko, et al., 2009)	
Figure 2.9 : Laboratory V _p -V _s data for water saturated shales (Mavko, et al., 2009)	
Figure 2.10 : Laboratory V _p -density data for shales (Mavko, et al., 2009)	
Figure 2.11 : Laboratory V _p -V _s data for water saturated limestones (Mavko, et al., 20	
Figure 2.12: Laboratory V _p -density data for shales (Mavko, et al., 2009)	
Figure 2.13: The histogram of compressional velocity (km/s) for 13 wells (Petrel 20)13)
Figure 2.14 : The histogram of shear velocity (km/s) for 13 wells (Petrel 2013)	
Figure 2.15: The histogram of density (g/cm3) for 13 wells (Petrel 2013)	
Figure 2.16: The histogram of Dynamic Young's modulus (GPa) for 13 wells (Petro	
2013)	
Figure 2.17: V _p -V _s cross plot (13 wells)	
Figure 2.18: V _p -density cross plot (13 wells)	
Figure 2.19: Young's moduli-depth cross plot (13 wells)	
Figure 2.20: Density- depth cross plot (13 wells)	
Figure 3.1: 3D model of study area with surface and bottom (pink) boundary (Petrel	
2013)	26
Figure 3.2: Pillar gridding and 2D window (Petrel 2013)	27
Figure 3.3: Layering and Geometrical modeling (Petrel 2013)	
Figure 3.4: Scale up well logs (Petrel 2013)	
Figure 3.5: Step-by-step workflow	
Figure 3.6: GRFS (left) and SGS (right) (Petrel 2013)	
Figure 3.7: Closest (left) and Moving average (right) (Petrel 2013)	
Figure 3.8: 3D model of Closest (left) and Moving average (right) (Petrel 2013)	
Figure 3.9 : Value distribution in 3D model of V _p (left) and V _s (right) in km/s	

Figure 3.10 : V _p value propagation in 3D model (km/s, Petrel 2013). (top view, b	ottom
view, north view, south view)	33
Figure 3.11: 3D model ran 100 times creating 100 realizations of the V _p value (I	km/s),
giving an "average" realization	33
Figure 3.12 : Uncertainty in 3D modeling of V _p value	33
Figure 4.1: Porosity-depth cross plot in sandstone section (numeration of well re	efers to
Table 2.1)	37
Figure 4.2: VASARI 001 DIR well section (DT, lithology, Young's modulus)	
Figure 4.3: Well cluster around VASARI 001 DIR well	39
Figure 4.4: Three scenarios for area of regional aquifer	39
Figure 4.5: CO ₂ density changes by depth (Benson et al., 2008)	
List of tables	
Table 2.1: Used well information	10
Table 3.1: Parameters for 3D model.	31
Table 4.1: CO ₂ injection criteria (Chadwick, et al., 2008)	34
Table 4.2: Well intersection with lithology	
Table 4.3 : Thickness and average porosity of sandstone (VASARI 001 DIR)	
Table 4.4 : Final results of effective storage capacity	

1. Introduction

a. Geology of the area

The Marche sector of central Italy, including Ancona and adjoining Adriatic self (Fig. 1.1), spans the transition from the outward-verging Northern Apennines fold-and-thrust belt to the flexural Adriatic foreland. In this tectonic context, inland anticlinal highs expose the Umbro-Marche pelagic and platform carbonates (Maiolica, Marne a Fucoidi, Scaglia), whereas basinward the succession grades into Miocene foredeep marls and siliciclastic turbidites of the Marnoso-Arenacea system and related units; these are overlain by thick Plio-Pleistocene marine muds widely mapped as the Argillle Azzurre (Fantoni & Franciosi, 2010) (Picotti, et al., 2007). The margin is not simply layered but segmented along strike: recent morpho structural analysis shows crustal-scale compartmentalization of the Umbria-Marche sector, with drainage metrics and topography capturing variation in uplift and confinement – an observation that helps explain shifts in sediment routing from the chain into foredeep; the synthesis figure used here from Teloni et al. provides a concise regional template for how sedimentation is organized in the study area (Teloni, et al., 2024).

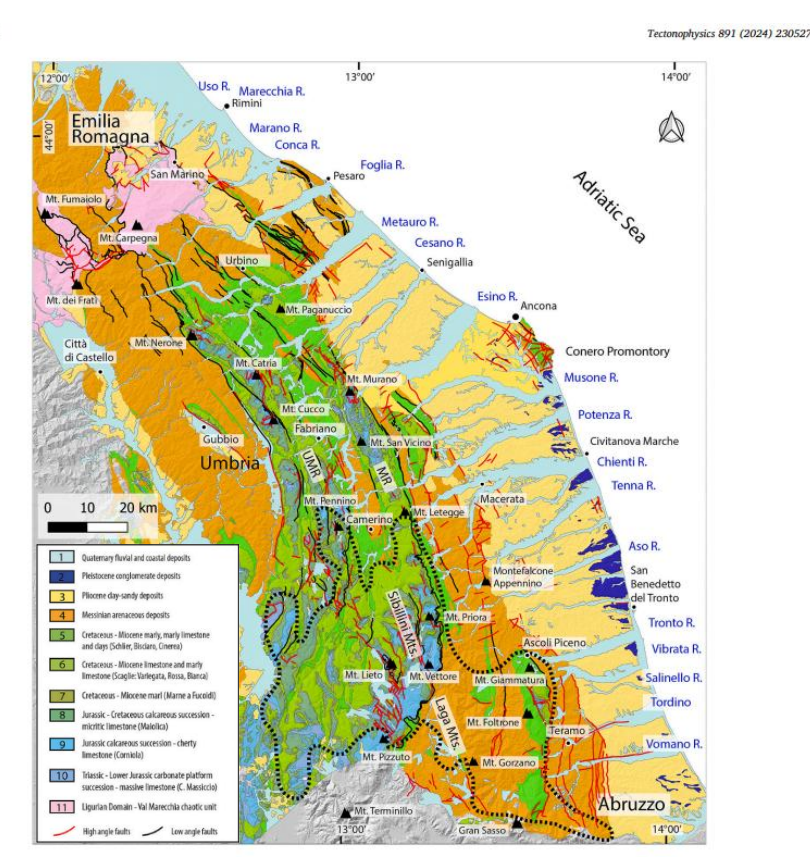


Figure 1.1: Geological sketch of UMAF (*Conti, et al., 2020*). The geologic units were grouped into 11 rock categories according to their lithology and stratigraphical position. Dotted black line limits the high Ksn value area.

At the scale of the northern Adriatic margin, late Quaternary "source-to-sink" reconstruction demonstrate how riverine supply, sea-level change, and shelf accommodation together carved a predictable onshore-to-offshore stratigraphic anatomy

from the Po Plain into the Adriatic Sea; those process links offer a modern analogue for interpreting shelf and offshore strata adjacent to Marche region (Amorosi, et al., 2015).

Ongoing tectonic subsidence in the shelf area in north of the Mid Adriatic Deep (MAD; Fig. 1.2) favored both the build-out and preservation of around 350 m-thick shallow Po-Delta, as well as a series of mud-prone regressive sequences that document the previous four 100-kyr (10³ years) climate-driven sea-level cycles south of the MAD. (Maselli, et al., 2011).

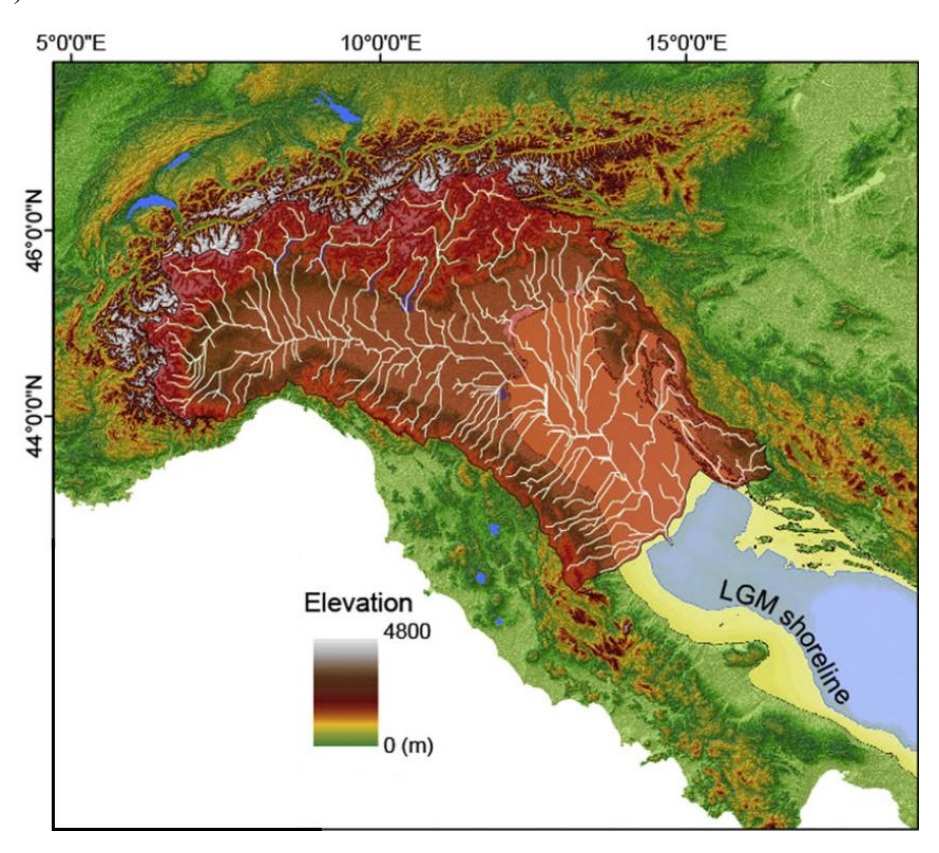


Figure 1,2: Inferred drainage directions, drainage areas and sediment discharge (Maselli, et al. 2011)

Beyond its academic appeal, the broader Adriatic domain has a long history of petroleum activity, with biogenic gas hosted in Neogene clastic and deeper oil in Mesozoic carbonates; legacy syntheses and exploration overviews frame the main structural styles and plays of this province (Oluić, et al., 2020). Natural seepage documented just offshore the Marche coast (near Civitanova Marche) indicates activation of fluid pathways in the shallow part of the subsurface; this underscore the importance of robust rock-property evaluation using data from wells here were drilled for diverse investigative purposes and not exclusively for hydrocarbon exploration (Cota & Baric, 1998).

Using public DT logs, the thesis evaluates geophysical and mechanical rock properties for the Marche-Ancona region - deriving V_p from DT and establishing empirical ties among V_p , V_s , density and elastic moduli - to deliver a regional, log-based property framework. While the study is not centered on storage applications, such a framework naturally complements legacy reservoir knowledge and can inform screening in mature or depleted intervals as part of broader geoenergy assessments in the area.

b. Scope of work

This thesis focuses on the evaluation of mechanical and geophysical properties of subsurface rocks in the Central-Eastern Italy and Adriatic offshore region through the analysis of publicly available well log data. The work uses a dataset containing sonic logs, from which compressional-wave velocity are derived, and lithology characteristics from drilling cuts. Direct measured density logs are not available in the dataset; therefore, bulk density is estimated using empirical velocity-density correlation from literature, with emphasis on regionally calibrated equation where possible. After performing modeling of the selected properties in a regional scale a stratigraphic interval was chosen for calculation of its CO₂ storage potential.

The current work is organized in the following steps:

- 1. Data acquisition and preparation-digitalization, identification of the available well logs. Import of DT logs data into Petrel software.
- 2. Velocity derivation estimation of shear-wave velocities using empirical relation suitable for the regional lithology.
- 3. Rock physical parameters calculation and correlation analyses- selection of empirical moduli to derive bulk density in absence of density log, determination of dynamic elastic moduli, statistical evaluation of relation between V_p and V_s, Young's modulus and density
- 4. 3D modeling of the studied area and distribution of the selected properties in Schlumberger Petrel software (v. 2013.1)
- 5. Analyzing CO₂ storage potential of a stratigraphic interval of the region, suitable for CO₂ storage.

2. Data used

This chapter presents the wells and logs used in the study, the steps taken to convert archived sonic records into analysis-ready data, and standards adopted for units, depths, and quality control. Publicly available well logs data offers only compressional sonic but not shear or density logs, therefore elastic properties are derived by applying lithology-based empirical relation to DT.

a. Wells

The working domain is the coastal-offshore region of the northern Marche, including the area around Ancona, northward from Pesaro and Urbino, southward to San Benedetto del Tronto, together with the adjoining mid-Adriatic shelf. The public well archive for the Marche-Ancona region is extensive: more than 150 wells are documented across the onshore and offshore sectors. Of these, 44 boreholes drilled between 1973 and 1997 include digitizable compressional sonic (DT) logs – 27 onshore and 17 offshore. To balance data quality with spatial coverage, the present work focuses on refined, evenly distributed subset of 13 wells – 6 onshore and 7 offshore – selected by following criteria:

- 1. Continuity and depth of DT across the targeted stratigraphy;
- 2. Geological coverage of the principal lithostratigraphic domains (shelf muds and sand, Miocene foredeep clastic, Mesozoic pelagic carbonates);
- 3. Log integrity, including coherent depth reference, acceptable image quality for digitalization, and absence of measuring tool problems.

Not all of the wells (150+) were drilled for the same purpose; if metadata were incomplete or log condition poor for reliable digitalization, candidates were excluded. The final group is evenly distributed across the area to avoid spatial bias. A location map (Fig. 2.1) shows well positions relative to the analysis polygon.



Figure 2.1: Study area in the northern Marche (Italy): costal line from Pesaro and Urbino to San Benedetto del Tronto with adjoining mid-Adriatic shelf. Green symbols indicate wells used in this study; the grey polygon outlines the analysis domain (Google Earth)

Table 2.1 Well name, coordinates, onshore/offshore setting, drilling year, KB and total depth of the wells used in this study.

No	Well name	Year	Latitude	Longitude	KB	Depth	Setting
					elev.	-	
1	RONCITELLI 001	1990	43.6955° N	13.1499° E	117	1630	onshore
	DIR						
2	ROSORA 001	1988	43.4958° N	13.0492° E	438	1688	onshore
3	VILLA FELICI 001	1997	43.6106° N	13.3239° E	26	1630	onshore
	DIR						
4	VASARI 001 DIR	1996	43.3905° N	13.5806° E	77	1130	onshore
5	PATERNO 001	1989	43.1794° N	13.3168° E	453	3628	onshore
6	S. PROCOLO 001	1986	43.1158° N	13.6239° E	175	2600	onshore
7	DORA 002	1995	43.1807° N	14.0863° E	26	1600	offshore
8	BREZZA 001	1985	43.6294° N	13.6253° E	28	1000	offshore
9	FIORELLA 001	1989	43.5192° N	14.1198° E	33	1600	offshore
10	CASSANDRA 001	1990	43.8591° N	14.1697° E	26	1300	offshore
11	BONAVENTURA	1981	43.8865° N	13.0172° E	25	3000	offshore
	001						
12	TAMARA 001	1987	43.9873° N	13.3406° E	25	3200	offshore
13	CARMELA 001	1987	44.1206° N	13.5849° E	27	1300	offshore

Table 2.1: Used well information

All wells depth reference is handled in MD from KB (measured depth referenced to kelly bushing). KB elevation is recorded in the headers. Geographic coordinates are stored in WGS84.

b. Well logs

The wells selected for the study share common limitations: the only measurement present systematically and at readable quality is compressional sonic data (Δt). other curves occur periodically and used qualitatively to support depositional environmental analysis and quality control. Herebelow there is the description of two representative samples (Fig. 2.2): one offshore (Carmela 001) and one onshore (Vasari 001 DIR), followed by a statement of the project-wide conventions for units and usage. Both profiles consist of two parts: (i) an upper header/interpretation panel that concentrate metadata, legends and small interpretive synopsis of the section; and (ii) the log tracks. Since the upper part mainly serves to interpret the lower part and format is almost identical across all profiles, we will focus on description of the lower part (log tracks).

Lithology line (left part). Patterns and formation names set out the framework for tops and assigning the identified facies.

SP. A spontaneous-potential curve used qualitatively to separate shale-prone from sand-prone intervals, to highlight bed boundaries and to check consistency against resistivity and sonic logs.

Resistivity (plotted on log scale). This part usually carries a single deep resistivity curve. In this study we use resistivity qualitatively: to confirm facies trends. Clean claystone tends to have higher resistivity than sand-rich intervals at similar depth, also to point out intervals where the response is clearly unstable or non-diagnostic (large oscillations, abrupt tool shifts, sign of invasion or poor borehole conditions).

Sonic Δt . After unit verification in the header, Δt is converted to V_p and becomes the starting point for all elastic properties. Both Carmela 001 and Vasari 001 DIRs' Δt axis has range of 190-90 $\mu sec/ft$.

Gas totale. A narrow column located at the left part; total hydrocarbon gas measured at the surface in the return mud during drilling. These are documented for context and are not used in the elastic-property workflow.

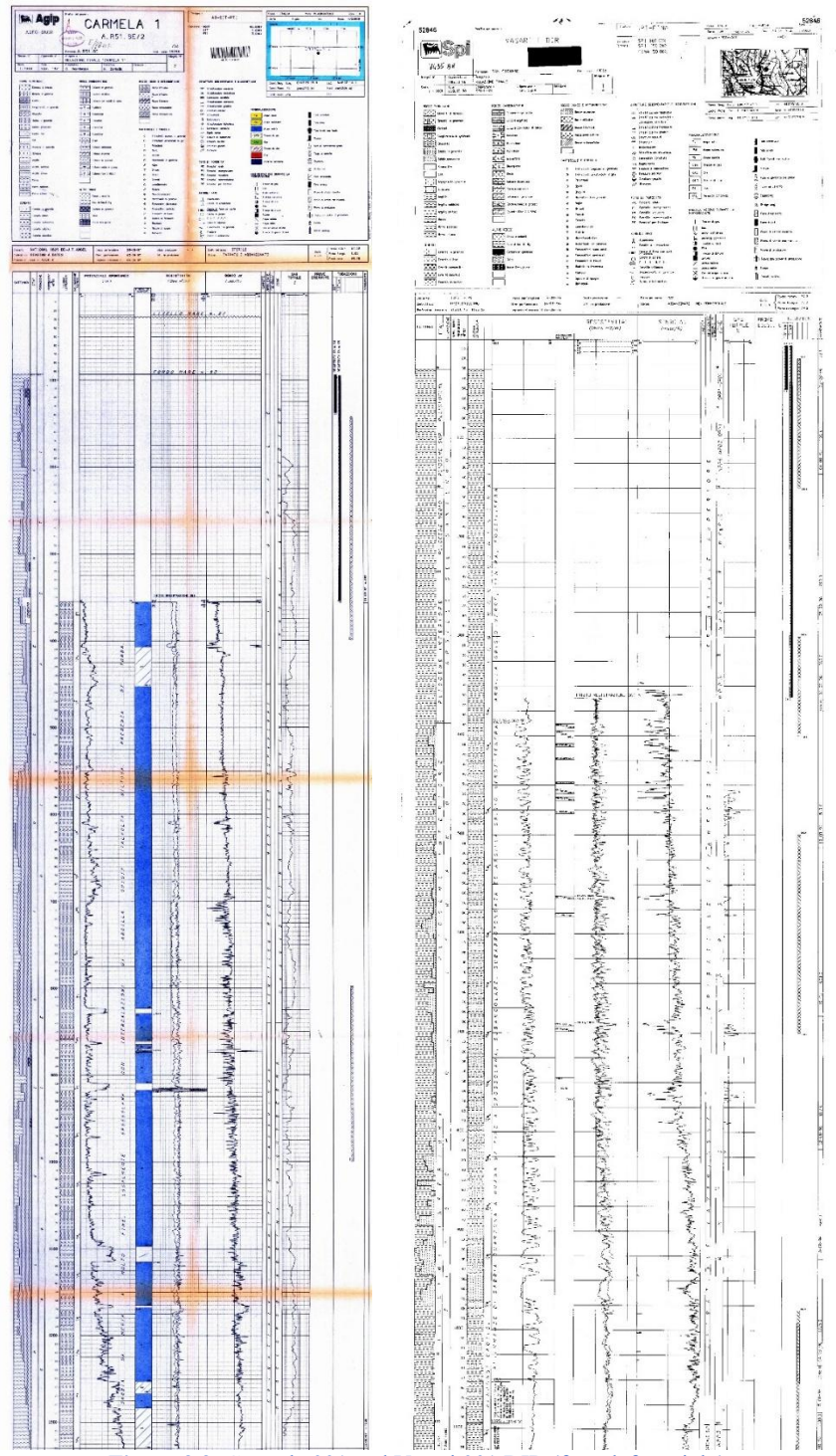


Figure 2.2: Carmela 001 and Vasari 001 DIR (from left to right)

c. Digitalization process

Digital depictions of well-log data produced over time are called raster well-log images. Pixels are a rectangular array of black (zeros) and white (ones) that represent bitmaps of the log image in raster digital well logs. Experts examine the raster logs by hand or using software programs that still need a significant amount of human input.

As we can see, the log dataset used in this study exists only as scanned raster images (PDF/TIFF). To make sonic travel time Δt usable for empirical work, the curve was digitalized and converted into numerical series sampled on a regular depth grid. The workflow is simple, reproducible, and explicitly limited: digitalized curve cannot be a perfect replica of the printed original, but the uncertainties are limited and managed.

Each log profile was exported at high resolution with maintaining proportion. Two axes were calibrated: (i) the depth axis using printed depth marks, and (ii) the Δt axis using scale marks. These control points define a piecewise-linear map from pixel coordination to physical values – depth (m) and Δt ($\mu s/ft$). A digitalizing routine followed DT trace and produced a dense set of points along the line (Fig. 2.3). Sometime panels contain notes, stamps or overlapping tracks, we need manually control points where the sonic line was interrupted or faint to keep the trace continuous. To preserve thin-bed details. No heavy smoothing or low-pass filtering was applied. In several well near surface readings sampled the casing/cement rather than the formation. Non lithological points were identified during QC and removed from the calculations.

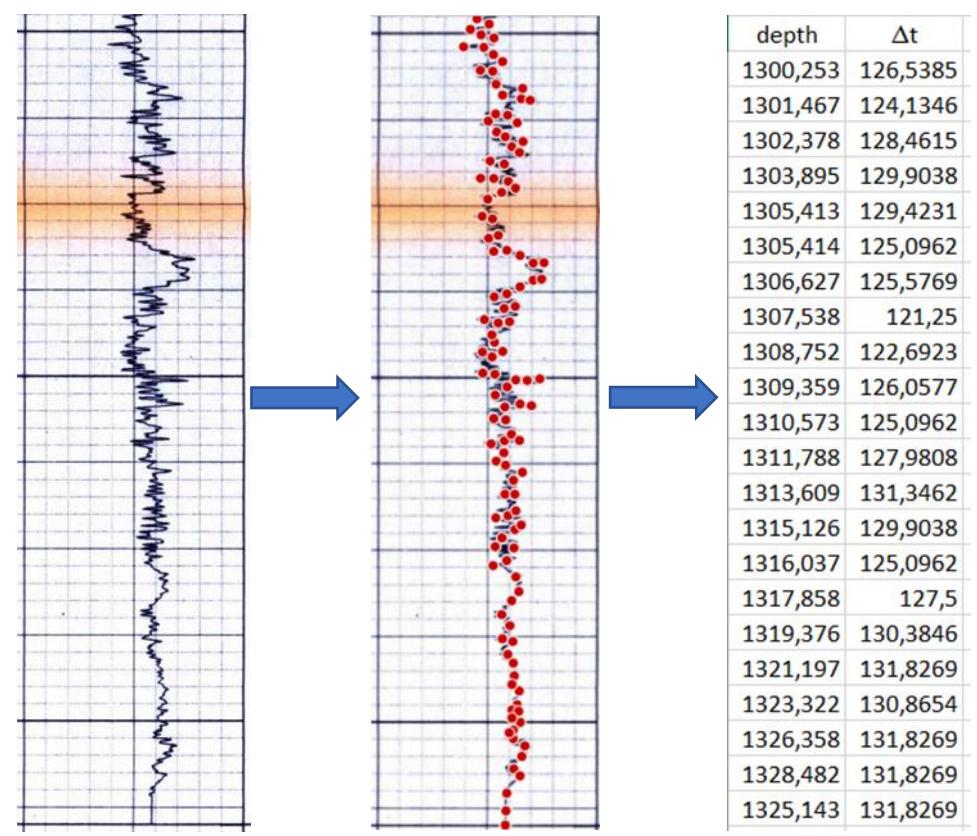


Figure 2.3: Steps of digitalization (section from Carmela 001)

To ensure unit integrity, trace fidelity, artificial removal, and physical plausibility, we applied Quality control to every digitalized curve as follows:

- Overlay check: the digitalized curve is over-plotted on the raster to confirm visual coincidence along the full depth (Fig. 2.4).
- Unit audit: Δt units are verified against header box before any conversion. Mismatched are corrected
- Physical bounds: values outside sedimentary ranges are reviewed rather than auto-accepted.

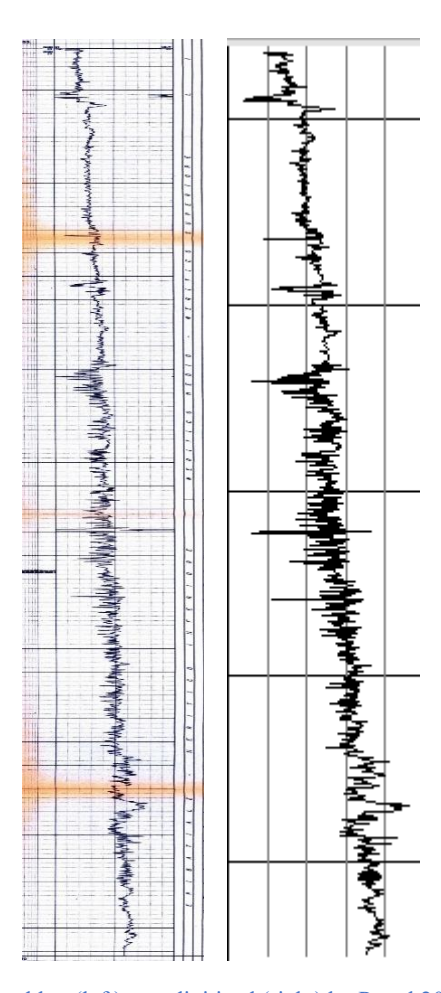


Figure 2.4: The photo-scanned log (left) was digitized (right) by Petrel 2013 (Carmela 001)

Digitalization cannot perfectly reproduce the printed curve because of (i) scan distortion, (ii) gridline thickness, (iii) line occlusions by notes or stamps, and (iv) finite pixel resolution. Automated methods improve throughput but still require human validation on ambiguous segments (Nasim, et al., 2023).

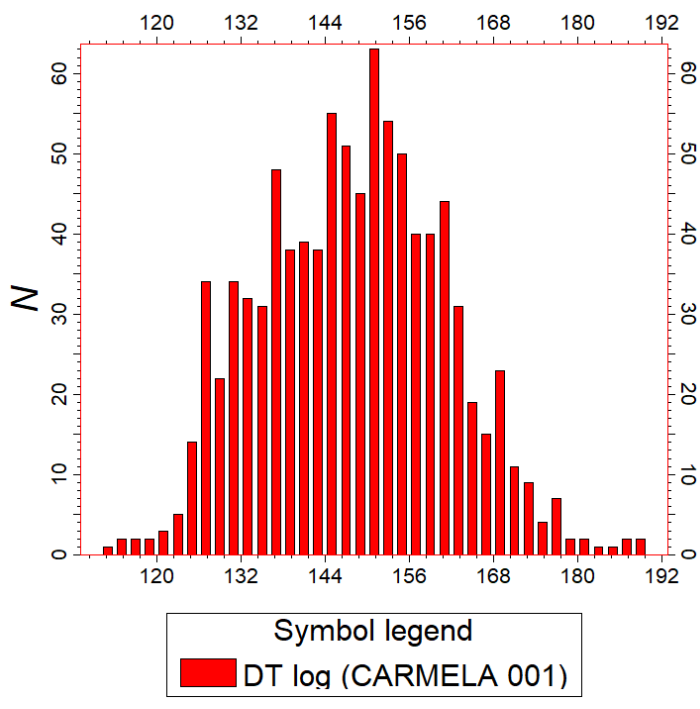


Figure 2.5: The DT (μs/ft) histogram of digitalized log (Petrel 2013)

The DT histogram for Carmela 001 (Fig. 2.5) shows a single, distinct peak with a near-Gaussian shape. Log values progressively rise from the lower tail at 118-122 μ s/ft, pass through a thick zone at 140-160 μ s/ft, and end in a narrow mode at 154-156 μ s/ft. Numbers drop evenly toward the higher tail, drifting by approximately 178-190 μ s/ft. The central part of the histogram is compact enough that neighboring bins show similar height, while both sides decay without "teeth" or step plateaus, which would imply grid misreads or mixed plotting scales. Overall, the histogram geometry aligns with expectations for an offshore mixed-siliciclastic section and provides a clean statistical foundation for further facies-aware methods.

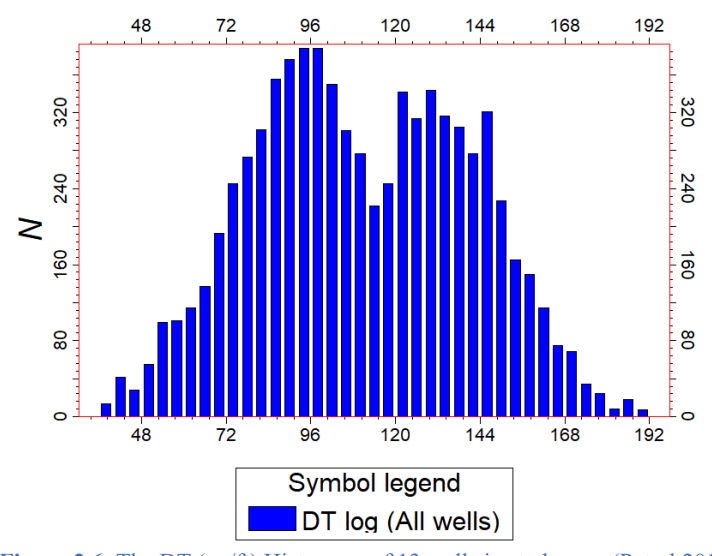


Figure 2.6: The DT ($\mu s/ft$) Histogram of 13 wells in study area (Petrel 2013)

The 13 wells' combined DT histogram (Fig. 2.6) does not display a single symmetric peak, but rather wide, somewhat bimodal distribution. Beginning at about 40-60 μ s/ft, counts grow at first peak at 95-100 μ s/ft, taper slightly around 110-120 μ s/ft, and then peak around 140-150 μ s/ft. After that, log values gradually decrease toward the high Δt , with few exceeding 170-190 μ s/ft. The low Δt tail, below 60 μ s/ft, is also thin. The pattern follows the stratigraphic characteristics: the fast mode (\sim 100 μ s/ft) reflects compacted sands and carbonates lines, while the slower mode (\sim 150 μ s/ft) reflects clay-rich and less packed intervals. The tails behave smoothly without combing or step plateaus, indicating a stable axis calibration across panel and no noticeable unit/scale mismatch. Overall, the aggregate distribution supports the expected facies mixture and depth compaction trends for the Marche coastal-offshore setting, with only a small fraction of samples approaching values \sim 190 μ s/ft that typically indicate very soft muds, gas effects, or local hole conditions rather than consolidated formations.

d. Use of empirical relations

The workflow begins with the transformation of the digitalized sonic travel time (DT) to compressional velocity (V_p) and then from V_p to shear velocity V_s , bulk density ρ , and dynamic elastic moduli. The approach is built specifically for the coastal-offshore zone from Pesaro/Urbino through Ancona to San Benedetto del Tronto and adjoining mid-Adriatic shelf, where public wells provide sonic travel time (DT) but luck shear (DTS) and density (RHOB) logs. Since the formations encounter sediments ranging from Plio-Pleistocene shelf muds and sands to Miocene foredeep clastic and Mesozoic pelagic carbonates, we rely on lithology-specific empirical transforms rather than single global equation. These transforms summarize large observation datasets and perform best for water-saturated rocks (Castagna, et al., 1985) (Han, et al., 1986) (Gardner, et al., 1974).

Units. All empirical coefficients are applied in their published units $-V_p$, V_s in km/s; ρ in g/cm3 – to avoid rescaling of the regressions. Before computing moduli, all quantities are converted to SI (m/s, kg/m3), and moduli are reported in GPa. This single, explicit conversion step prevents unit drift between logs, transforms and property calculations.

Lithology framework. Every depth sample is classified from the lithology track and stratigraphy into sandstone, claystone, sandy clay (mixed shaley sandy mud) or limestone. These partitioning honors first-order differences in frame stiffness, clay content, mineralogy and expected compaction state that would otherwise be averaged away by a universal transform. It also reflects the reality of the region: Argille Azzurre and related muds (claystone), shelf sands (sandstone), mixed shallow – upward units (sandy clay), and deeper pelagic carbonates (limestone).

In order to derive compressional velocity from sonic travel time, units of measurement need to be changed from $\mu s/ft$ to km/s:

$$V_p = 304.8/DT [km/s]$$

Sandstone (clean to low – shale siliciclastic)

For sand – prone siliciclastic under brine saturation, the equation provides a first-order relation between V_p and V_s (Castagna, et al., 1993):

$$V_s = 0.804 \times V_p - 0.856 \ [km/s] \tag{1}$$

This line (Fig. 2.7) captures the stiffer elastic response of well sorted sands relative to mudrocks and has been widely adopted for AVO/AVA, impedance, and rock-physics workflow where shear logs are unavailable. In our study area, it suits inner to mid-shelf setting where bioturbation and moderated cementation stiffen the frame without introducing strong carbonate mineralogy.

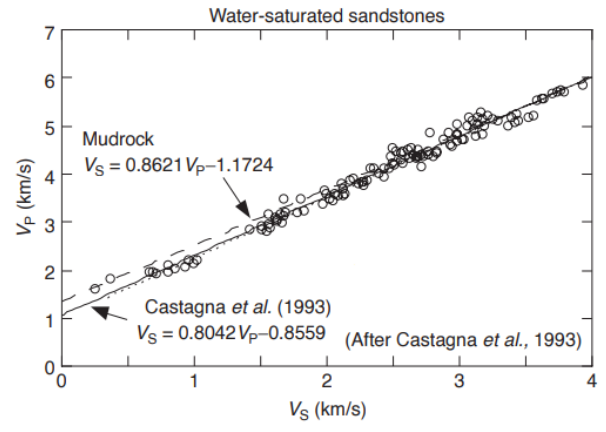


Figure 2.7: Laboratory V_p-V_s data for water saturated sandstone (Mavko, et al., 2009)

As a density relation for sandstone, we apply following equation of Gardener (Gardner, et al., 1974):

$$\rho = 1.66 \times V_p^{0.261} \ [g/cm^3] \tag{2}$$

which remains the simplest and most reproducible choice in the 1.5-6.0 km/s range typical of Plio-Pleistocene and Miocene siliciclastic. Both forms of Gardener's relations (Fig. 2.8) applied to laboratory sandstone data as presented by Castagna (Castagna, et al., 1993). As we can see both equations have same prediction for real data.

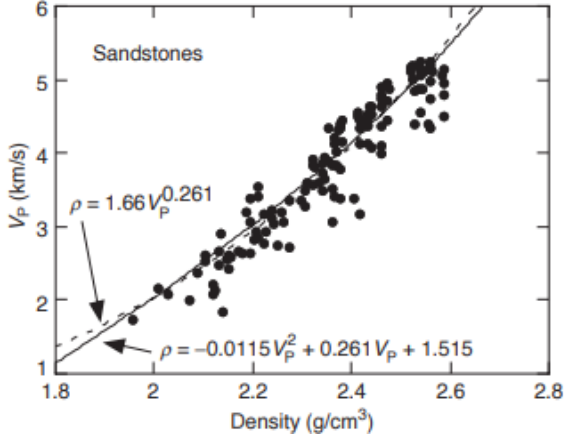


Figure 2.8: Laboratory V_p-density data for sandstone (Mavko, et al., 2009)

Claystone (mudrock/shale)

Clay-dominated intervals – high gamma ray, low resistivity and log consistent with Argille Azzurre and other foredeep muds – are mapped with the following equation (Castagna, et al., 1985):

$$V_s = 0.862 \times V_p - 1.172 \ [km/s]$$
 (3)

The laboratory data form a linear relationship (Fig. 2.9) that predicts the central tendency of the measurements.

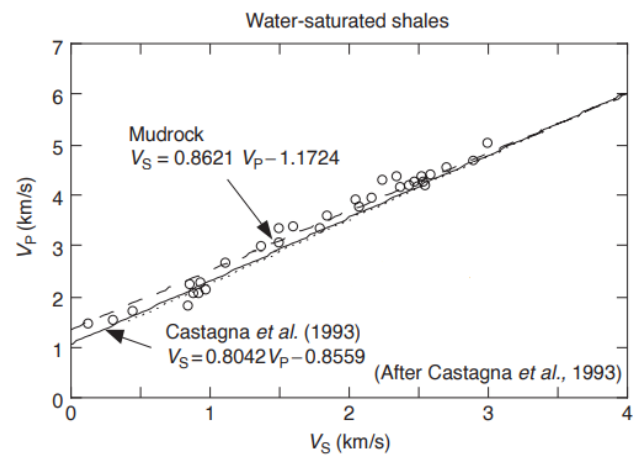


Figure 2.9: Laboratory V_p-V_s data for water saturated shales (Mavko, et al., 2009)

Density follows Gardener equation for shale (claystone as followed (Gardner, et al., 1974).

$$\rho = 1.75 \times V_p^{0.265} \ [g/cm^3] \tag{4}$$

Both forms of Gardener's relations (Fig. 2.10) applied to laboratory shale data as presented by Castagna (Castagna, et al., 1993). Compared with high-order fits, this simple relation is stable and reliable. It captures compaction across velocity range while avoiding overfitting at the tails.

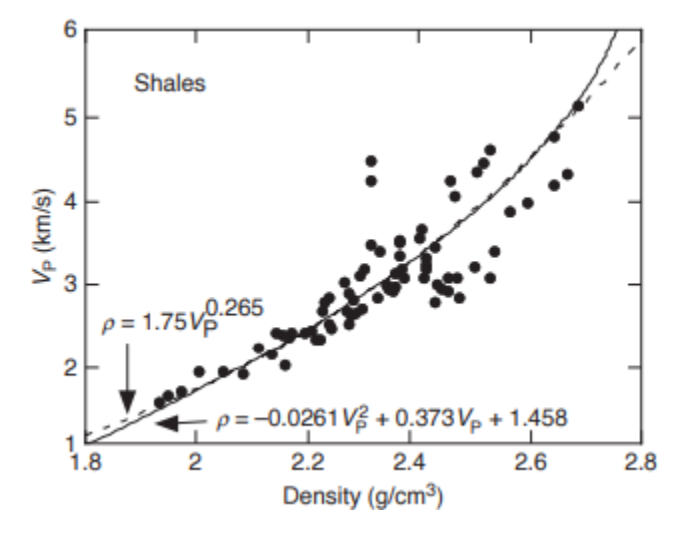


Figure 2.10: Laboratory V_p-density data for shales (Mavko, et al., 2009)

Sandy clay (mixed shaley sand/sandy mud)

Mixed facies are ubiquitous in the study area (e.g., sandy muds in upward-coarsening packages). Rather than forcing an explicit mixing algorithm that requires mineral fractions, this study adopts a single empirical midline that adopt am intermediate regression defined as the arithmetic mean of the published sandstone and mudrock relations (Castagna, et al., 1985), keeping predictions between the two end-member families.

$$V_s = 0.833 \times V_p - 1.014 \ [km/s]$$
 (5)

This "sandy-clay midline" acknowledges the well documented tendency for increasing clay content and lower effective pressure to reduce V_s at fixed V_p relative to clean sands while avoiding the sensitivity of fraction-based mixing to noisy shale estimates in shallow, under-compacted sections (Han, et al., 1986). In practice it functions as a balanced backbone for mixed facies: intervals that truly behave like end-member sands or shales still cluster around the sand or mudrock lines, whereas genuine sandy-clay points occupy a stable band around the midline.

For density, defensible "midline" for sandy clay is the geometrical mean of two clastic laws with the average exponent (Gardner, et al., 1974):

$$\rho = 1.704 \times V_p^{0.263} \ [g/cm^3] \tag{6}$$

This formula lies between sandstone and claystone for mixed fabrics of 30-60% clay, may have uncertainties relative to the end-member trends.

Mixed intervals are expected to fill the space between the sand and mudrock families on V_p - V_s , V_p -density plots; depth trends typically show progressive tightening of the spread with compaction. Any 'cups' or 'loops' in-depth trajectory usually shows facies misclassification or local tool/environment effects (washout, cycle skipping).

Limestone (pelagic carbonates: Scaglia, Maiolica)

Carbonates in the – pelagic limestone of the Scaglia and Maiolica succession – do not follow clastic velocity trend. Therefore, we use the monomineralic regression for limestones (Castagna, et al., 1993):

$$V_s = -0.0551 \times V_p^2 + 1.0168 \times V_p - 1.0305 \ [km/s] \tag{6}$$

The Castagna (Castagna, et al., 1993) polynomial (Fig. 2.11) passes through the center of the cloud and captures the slight upward curvature at higher velocities that (Pickett, 1963; Fjaer, et al., 2008) line misses.

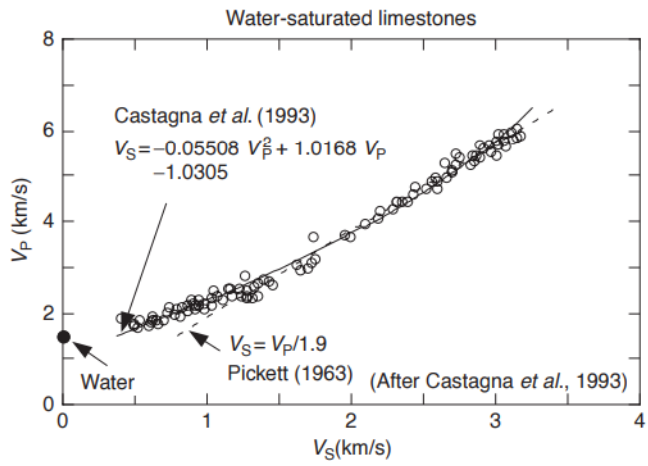


Figure 2.11: Laboratory V_p-V_s data for water saturated limestones (Mavko, et al., 2009)

As a density path we continue to use Gardener equation but for limestones as followed (Gardner, et al., 1974):

$$\rho = 1.36 \times V_p^{0.386} \ [g/cm^3] \tag{7}$$

Compare with the quadratic alternative (Fig. 2.12), the power law is simpler and less prone do edge effects, yet it preserves the upward curvature associated with increasing lithification and cementation.

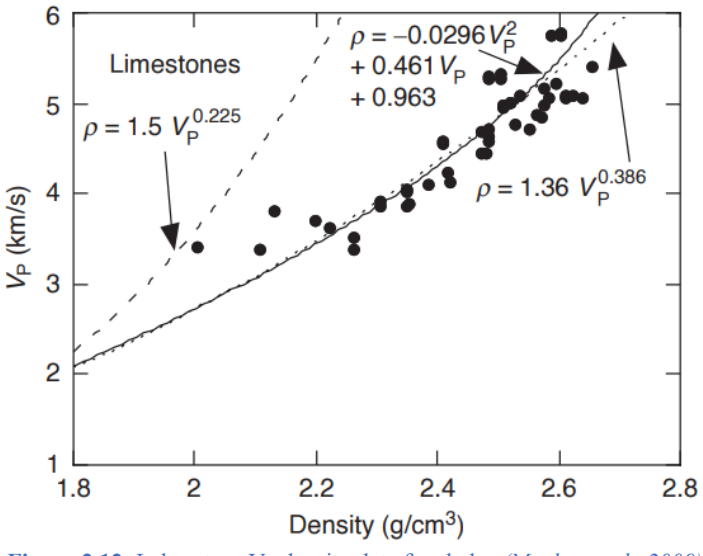


Figure 2.12: Laboratory V_p-density data for shales (Mavko, et al., 2009)

Carbonates need extra interpretive care. Heterogeneity (e.g., stylolite, micro-fracture, early diagenetic cement) can produce scale-dependent responses that differ between sonic and seismic band. Moreover, dolomite (if present) has its own linear relation and should not be forced into the limestone polynomial. Where dolomite is suspected from logs or regional mapping, intervals are reclassified accordingly.

Young's Moduli

In this thesis dynamic Young's modulus E is computed directly from acoustic velocities and density

$$E = \rho \times V_s^2 \times \frac{3V_p^2 - 4V_s^2}{V_p^2 - V_s^2} \qquad [Pa]$$
 (8)

with V_p and V_s in m/s and ρ in kg/m³ (output in Pa; reported as GPa). This expression follows linear-elastic, isotropic wave theory and standard in rock physics and petroleum geomechanics for converting log-scale velocities into dynamic elastic properties (Fjaer, et al., 2008).

Young's modulus is the axial stiffness of the rock; the ratio of uniaxial stress to uniaxial strain. Higher E means the formation deforms less for the same applied stress. In the velocity form used here, E is especially sensitive to V_s (note the V_s^2 multiplier), so clayrich, under-compacted intervals with lower shear velocity have lower E, whereas well-sorted sands and carbonates with higher V_s have high E. The V_p term contributes mainly through the rock's compressibility, so constrains in V_p/V_s map directly compares with contrast in stiffness, it's useful for ranking lithologies and for onshore-offshore comparison across the Marche region.

Results of empirical relation

 V_p distribution (km/s) for all 13 wells is shown in Fig. 2.13 with dominating mode about 2-2.4 km/s, a broad shoulder through 2.6-3.6 km/s, and long tail that reaches 6-7.5 km/s. This is mostly expected for northern Marche coastal-offshore sector: better compacted clastic (foredeep marls and turbiditic sand) are captured by shoulder, whereas Mesozoic carbonates (limestone) and locally cemented units are represented by the high velocity tail. The pattern reflects Plio-Pleistocene shelf muds and silts as well as fine, water-saturated sands.

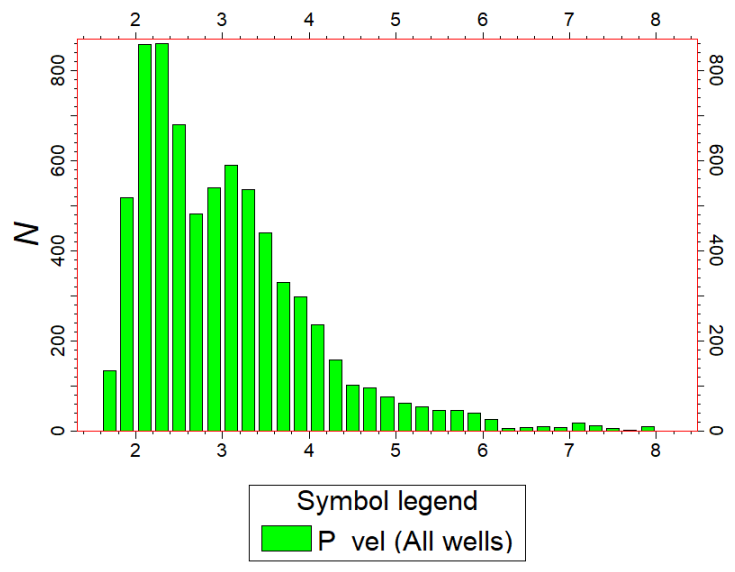


Figure 2.13: The histogram of compressional velocity (km/s) for 13 wells (Petrel 2013)

The stacked V_s spectrum for 13 wells (km/s) is weighted toward low velocities (Fig. 2.14). Values below 0.4 km/s are rare. Numbers peak around 0.8-1.0 km/s, then second rising through 1.2-2.0 km/s and drop off to individual occurrences near 3.2-3.4 km/s. Geologically speaking, this indicates that the shallow portion of the column is dominated by silty units and immature marine muds, with cleaner or more compacted sands providing a mid-range shoulder and isolated stiff carbonate layers producing the high V_s .

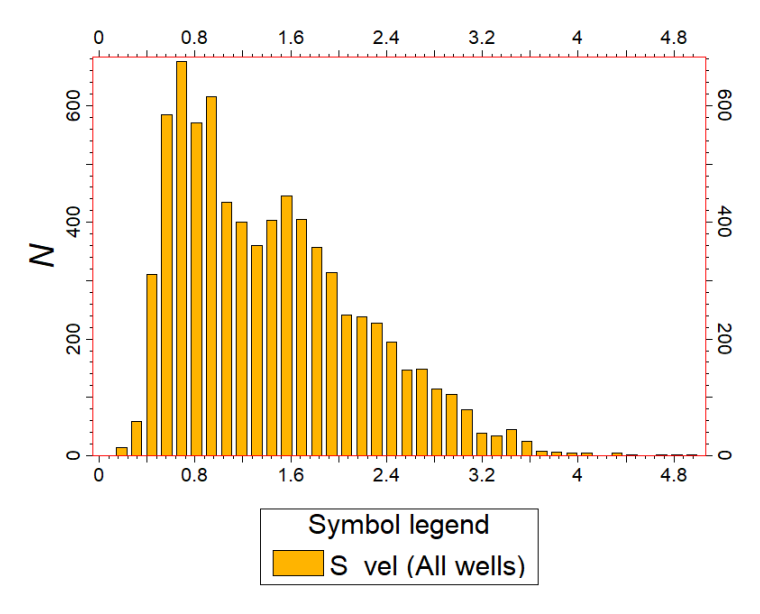


Figure 2.14: The histogram of shear velocity (km/s) for 13 wells (Petrel 2013)

The density of the samples sits between 2.0 and 2.45 g/cm³ (Fig. 2.15), with a sharp crest near 2.1 g/cm³ and subsequent increment near 2.3 g/cm³, then steadily thinning tail that reaches 2.7-2.8 g/cm³. The mode of the histogram near 2.1 g/cm³ reflects Plio-Pleistocene shelf muds and silty clastics with high water content; the mid-range is typical for cleaner or more compacted sands and marls; and the sparse heavy tail (~2.75 g/cm³) corresponds to carbonate beds.

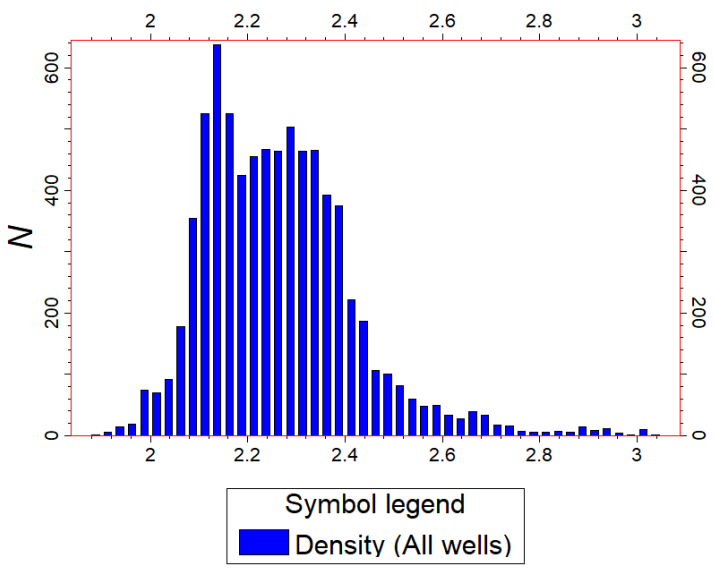


Figure 2.15: The histogram of density (g/cm3) for 13 wells (Petrel 2013)

Dynamic Young's modulus E (GPa (Morteza, et al., 2020)) for the 13 wells is highly right-skewed (Fig. 2.16): most samples fall below 25-30 GPa, with frequency dropping rapidly through 30-40 GPa and only a thin tail reaching 80-120 GPa showing abundance of clastic sediments in the upper portion of the area that progressively compact and become denser with depth producing higher E values.

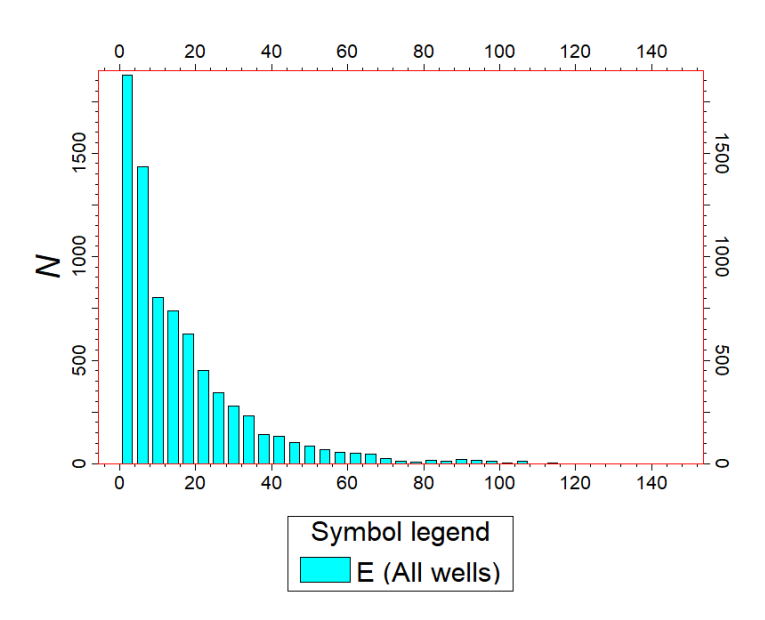


Figure 2.16: The histogram of Dynamic Young's modulus (GPa) for 13 wells (Petrel 2013)

The V_p - V_s graph (Fig. 2.17) reveals an evident clastic behavior limited by sandstone (lower V_p / V_s) and mudrock (higher V_p / V_s). Sand-flagged points cluster along the lower line because a quartz-rich frame sustains shear well; claystone sits near the upper line where bound water and platy grains weaken the frame, so V_s grows more slowly than V_p . Interval tagged sandy clay fill the narrow band between the two lines, forming a continuous transition rather than separated cluster – exactly what a mixed sand-shale should produce. The curves bend gently at low velocities (roughly V_s below 1 km/s, V_p near 2 km/s), reflecting under compacted shallow section where fluid supported V_p falls less steeply than frame controlled V_s .

Carbonates separate distinctly from clastic: for the same V_s , they plot higher V_p , following the limestone trajectory. Tight micritic or spar-cemented beds push the cloud upward (high V_p) while keeping V_s comparatively strong, so the ratio V_p/V_s stay low-moderate but the absolute speeds are high. The place where the limestone markers drift back toward the clastic band, that usually reflects marly or chalky texture or thin calcarenites interbedded with mud. In the Marche area this behavior is expected for Scaglia type pelagic carbonates. Mostly Paterno 001, Brezza 001, Bonaventura 001 wells reaching large limestone layers.

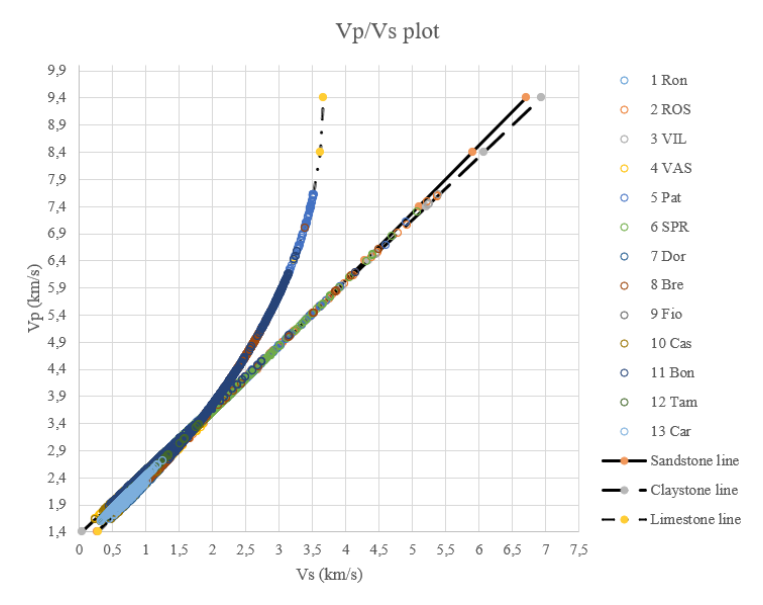


Figure 2.17: V_p-V_s cross plot (13 wells)

The V_p -density cross-plot organize the data into expected facies families (Fig. 2.18). Sandstone follows the lower branch (higher V_p at given density because the shear frame is stiffer), claystone tracks the upper branch (V_p rises more slowly), and sandy-clay fills the space between them as a smooth transition. The cloud bends upward with increasing density (classic compaction behavior). Shallow, water-rich clastic group around 1.9-2.2 g/cm³ with modest V_p , and progressively denser, better packed intervals toward higher V_p at 2.4-2.8 g/cm³.

Carbonates (limestone) peels away from the clastic regression: for the same density they plot at higher V_p , reflecting their stiff mineral frame and cementation; the limestone trend is therefore offset toward the high-velocity side. Cementation and recrystallization stiffen the frame much faster than bulk density changes, driving V_p sharply upward at nearly constant density. As a result, the limestone curve steepens and intersect sand-shale trends at intermediate densities.

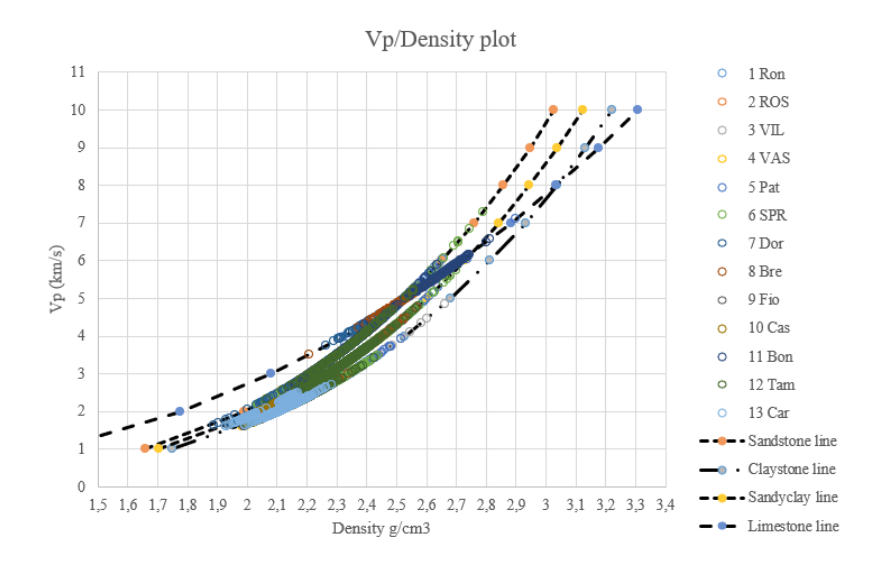


Figure 2.18: V_p-density cross plot (13 wells)

Dynamic Young's moduli (E) derived from sonic logs as a function of depth for 13 wells (Fig. 2.19). Values were computed from V_p , V_s and density assuming linear isotropic elasticity (8). Depth is referenced to KB; modulus is reported at log sampling without smoothing to preserve stratigraphic variability.

The data group displays the expected mechanical stiffening with burial: shallow intervals (0-500m) cluster mostly less than 20-30 GPa, consistent with unconsolidated to weakly cemented sands, marls and claystone. Between 1200-2000 meters the cloud broadens to 20-50 GPa as compaction and cementation increase. Below 2500 meters many samples lie in the range of 20-70 GPa, consistent with tight sandstone and carbonates, but also sandy clay in some parts. Most wells follow the burial with overlapping envelopes; however, Well '2 Ros' forms a distinct high-modulus cluster (20-45 GPa above 250 m). This behavior is lithology-controlled and consistent with the log description: plastic calcareous clay with abundant debris consisting of mollusk shell, locally abundant lignite and mica are present (0-167 m), grading into light brown sandstones with carbonate cement with passage to soft calcarenites (167-230 m) (ROSORA 001, 1988). At fixed depth, expected rock type: claystone/mudrock populate the upper part of envelope (low E), sandstones occupy an intermediate band that shifts right, limestone intervals plot at the stiff end (high E). Low E within deep sections likely mark porous streak, weak cement, or gas effects; conversely, high E spikes at moderate depth indicate locally well-cemented tight sandstone beds.

These moduli are dynamic and typically exceed static laboratory module by 1.5-2 time depending on lithology and stress state (Morteza, et al., 2020).

Depth/Young's moduli

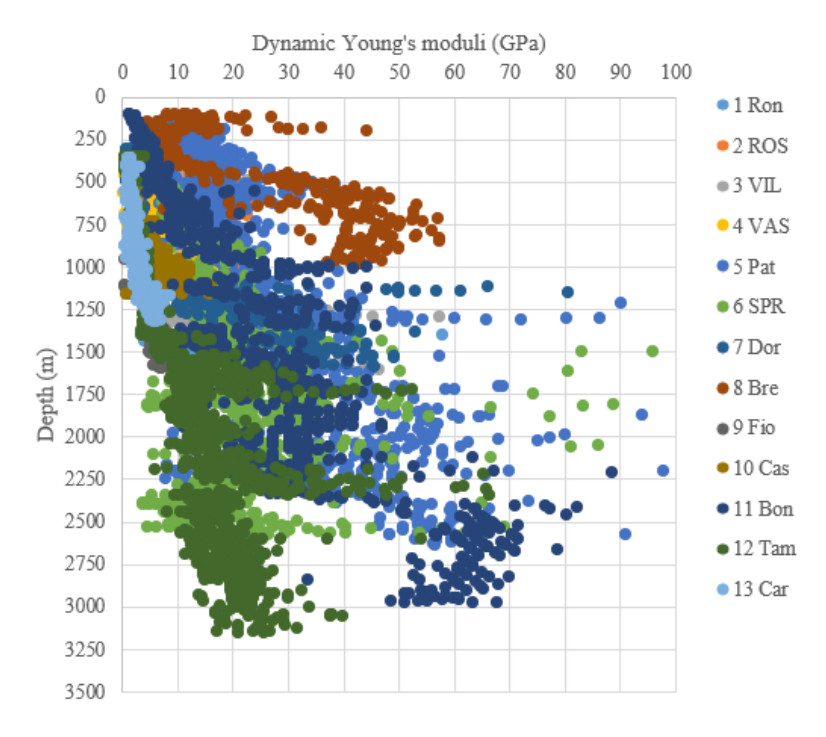


Figure 2.19: Young's moduli-depth cross plot (13 wells)

The cloud exhibits the expected rising density with burial (Fig. 2.20): near surface interval cluster around 2-2.2 g/cm³, then progressively tighten toward 2-4-2.7 g/cm³ by 1000-2000 meters as mechanical compaction, porosity loss, and early cementation take place. At greater depth (above 2500 m) densities locally exceed 2.7 g/cm³, consistent with well-cemented sandstone and carbonates. Overall, the density – depth behavior is internally consistent with the Young's modulus result (Fig. 2.19) and supports a burial-controlled stiffening trajectory modulated by lithology and cementation.

Depth/Density

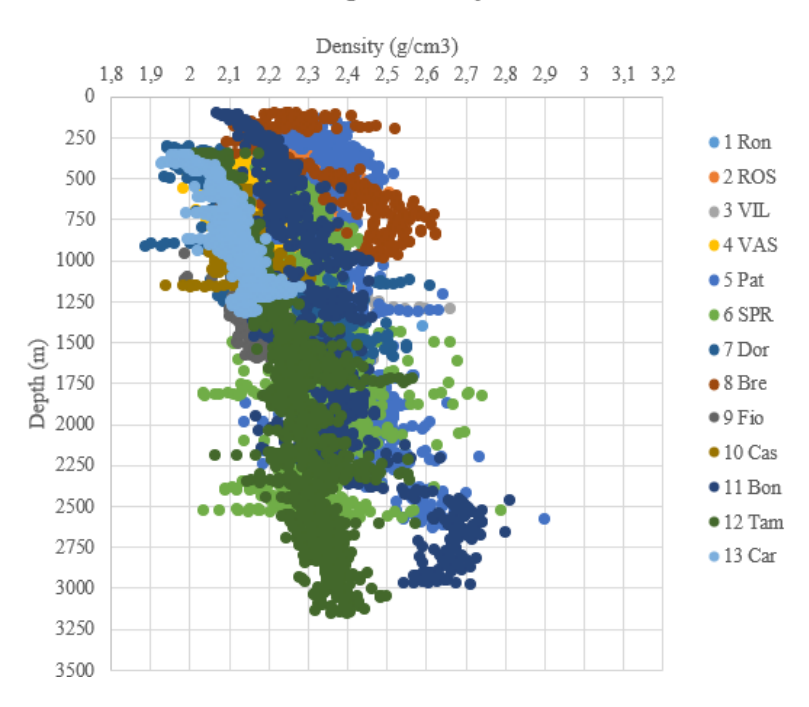


Figure 2.20: Density- depth cross plot (13 wells)

3. Model construction

All subsurface modeling in this thesis was carried out in Schlumberger Petrel (v2013.1) software, a workflow-oriented platform that integrates well data, seismic interpretation, stratigraphic frameworks, and property modeling within a single project. Petrel was used to (i) construct the structural framework (faults, key horizons) and discretize it into geologically meaningful zones/layers; (ii) manage well data – import of Δt and derive histogram and curves (Vs, Vp, ρ , E) and basic QC; and (iii) populate the grid using alternative distribution schemes with explicit control of variograms, search neighborhoods, trends, and random seeds.

a. Description of the model

The polygon area is approximately 14 456 km² with a vertical model height of 4.6 km (600 m above sea level, 4000 below sea level), the computational domain's rock-volume total, before masking the water column and any out-of-framework cells is near 66 500 km³ (Fig. 3.1). The active volume decreases during seabed masking and coastal clipping (offshore/onshore outline).

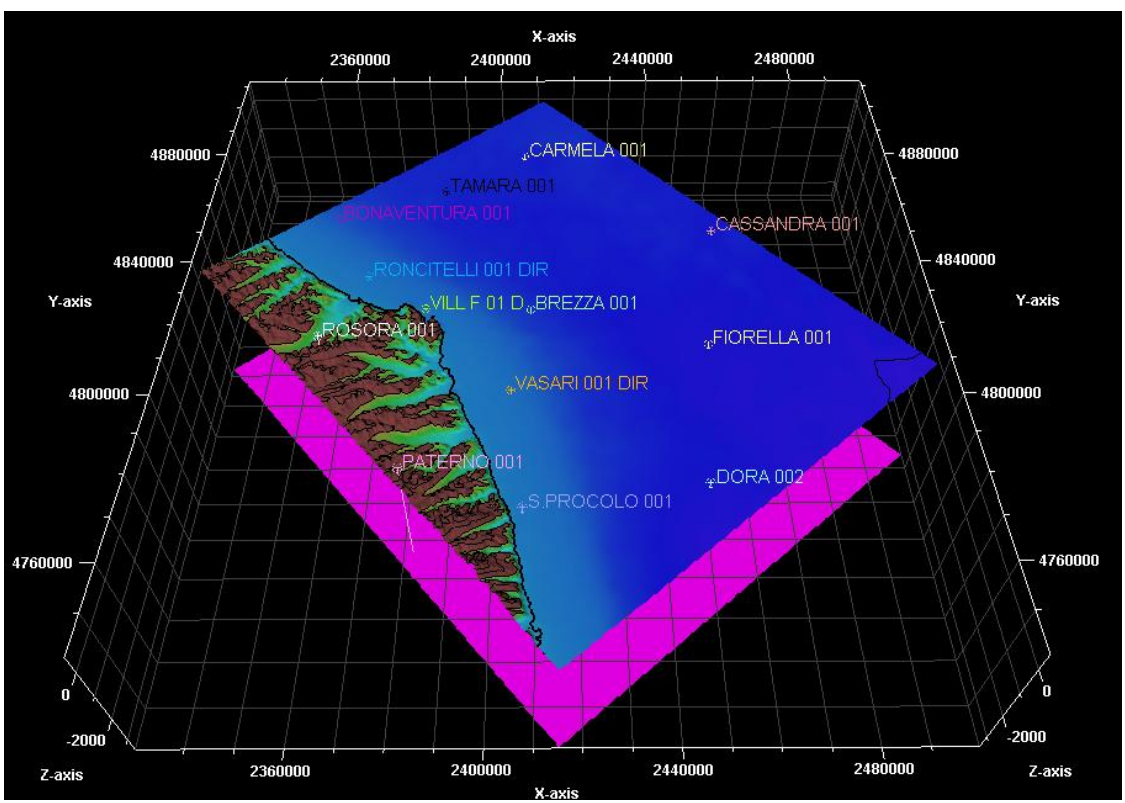


Figure 3.1: 3D model of study area with surface and bottom (pink) boundary (Petrel 2013)

The geocell framework is constructed as a corner-point (pillar) grid that conforms to the mapped structure within the study polygon. All plan-view calculations are performed in WGS-84/UTM 33N so that lateral dimensions are expressed in meters, while depths are referenced to TVDSS (m, positive downward). By spanning pillars between the model's top and bottom surfaces, Petrel generates a corner-point grid that accommodates gentle structural dip and curvature yet remains metrically consistent.

Lateral resolution is controlled by the chosen I-J increments (meters), which act as target cell sized in the east-west and north-south directions (Fig. 3.2). Smaller increments sharpen the capture of well-scale heterogeneity and coastline details, but increases number of cells thus time for constructing model, whereas large increments trade details for efficiency and continuity. To avoid directional bias during property propagation, the spacing in I and J kept broadly comparable (1:1) and aligned with the principal structural grain of the area and chosen as 500x500.

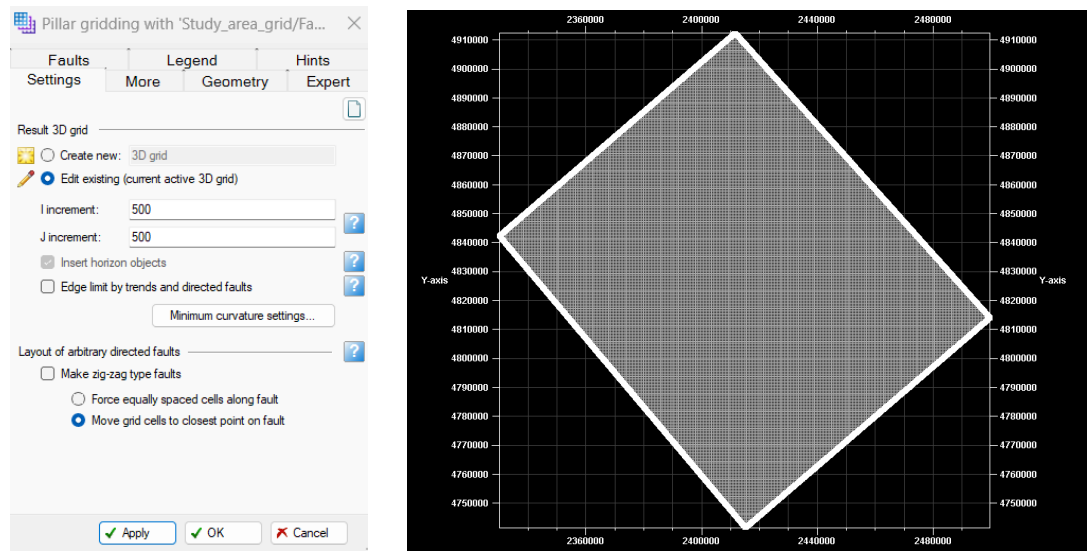


Figure 3.2: Pillar gridding and 2D window (Petrel 2013)

Vertical resolution is introduced independently through K-layering, which slices each column between surface and bottom boundary at 4 600 m TVDSS. It is portioned into 100 layers (Fig. 3.3), giving an average nominal thickness of 46 m per layer.

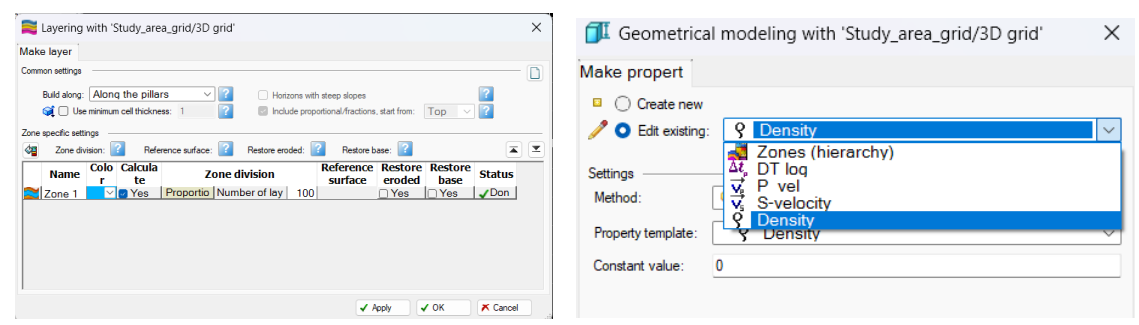


Figure 3.3: Layering and Geometrical modeling (Petrel 2013)

Geometrical modeling (Fig 3.3) promotes the interpreted well curves from Petrel's input plane into the active Model framework, aligning them to the project CRS, datum, and the established pillar grid. Surfaces are confirmed to the grid and layers are instantiated, so log data reference in TVDSS. This handoff provides the consistent geometry required for log upscaling and subsequent 3D property distribution.

Log upscaling (Fig 3.4) converts depth-sampled well curves into cell-based (upscaled) logs on the established pillar grid, consistent with model's I-J-K resolution and active-cell mask. Continuous properties (DT, V_p, V_s, density, Dynamic Young's modulus) are aggregated with thickness weighting within each intersected cell.

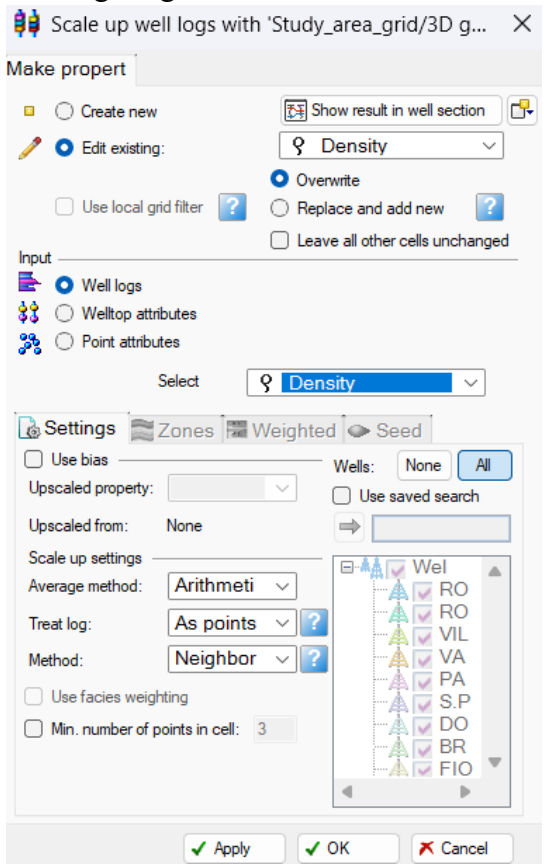


Figure 3.4: Scale up well logs (Petrel 2013)

Petrophysical modeling distributes the cell-based values (DT, V_p, V_s, density, Dynamic Young's modulus) from the upscaling stage through the grid to form continuous 3D property fields, while keeping the model portioned by zones and facies so the clastic and the carbonate behaviors are propagated within their own frameworks. Only active cells inside the study boundary are considered. Directional continuity is controlled with anisotropy information (variogram) expressed in meters: Major range, Minor range, and Vertical range. The major range is aligned with the dominant continuity of the system (along strike), the minor range lies perpendicular to it in map view (across strike), and vertical range follows the layering (TVDSS). Nugget and total sill set small-scale variability and overall variance, while three directional ranges govern how that variance is expressed in space during propagation. Fig. 3.5 provides a step-by-step overview of the modeling workflow. This visual sequence clarifies how well-derived values are transfer to 3D.



Figure 3.5: Step-by-step workflow

b. Different methods used for value distributing

Available property distribution models in Petrel 2013 include: Kriging (deterministic), Moving average, Functional, Closest, Assigning values, Neutral net, User defined algorithm. Methods shown in this paragraph give us more realistic value propagation (checked by histogram). For simplicity only P-wave velocity will be used as compare parameters.

Gaussian random function simulation (GRFS, unconditional). Used to generate prior spatial structure that matches the variogram (nugget, total sill, major-minor-vertical ranges) forcing exact reproduction of the well control points. In dataset with sparse and uneven control, GFRS provides a neutral baseline for sensitivity tests and scenario bracketing; it reduces the risk of overconfident smoothing when the underlying trends are not well defined. Histogram (Fig. 3.6) shows V_p value distribution across 3D in % (P_vel), alongside with well data (Well logs) and scaled up well log data (Upscaled cells) when we applied GRFS. Although upscaling shows some decreasing compare to well log data, GFRS more or less respects well data values.

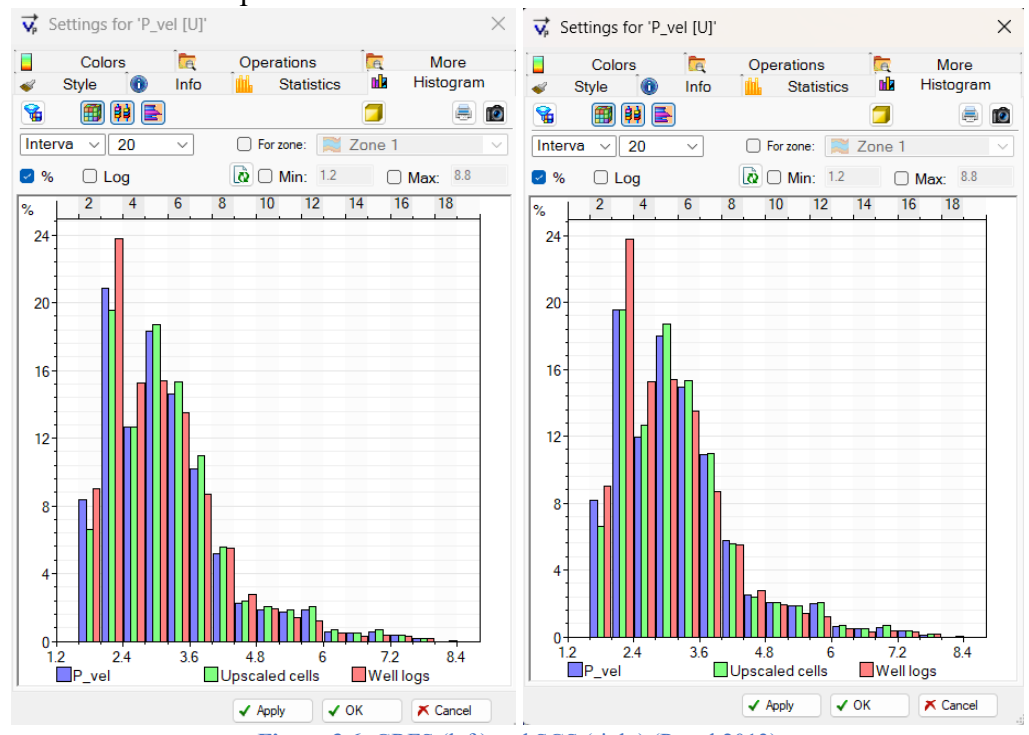


Figure 3.6: GRFS (left) and SGS (right) (Petrel 2013)

Sequential Gaussian simulation (SGS, conditional). Used to generates multiple, equiprobable 3D realizations by normal-score transforming data, sampling each cell from the local conditional distribution implied by the variogram and nearby well data, then back-transforming to physical units; this preserves the histogram, honors local extremes, and propagate anisotropy continuity. Unlike GRFS, which matches the variogram without conditioning to wells and thus provide a baseline continuity model, SGS is fully conditional, so the variability it produces is data-honoring and directly usable for heterogeneity and risk assessment. Histogram (Fig. 3.6) shows value after using SGS distribution in 3D scale. It shows more dependents to upscaled data (Upscaled cells) rather than well data itself (Well logs).

Closest (nearest-neighbor). Applied as hard, local assignment, useful as facies initialization and for producing contrast maps that preserves sharp, well-centered features. In this work it serves as diagnostic fundament to the stochastic simulation, revealing where smoothing would blur geological meaningful contrasts. It chosen here for its transparency and speed during method comparison. It operates by assigning each active cell the value of the nearest well sample within 3D search neighborhood, using straight-line distance in model space. Histogram of this model distributed property (Fig. 3.7) shows some high number of values in percentage in respect to the well and to upscaled data, which leads to sharp transition between properties (Fig 3.8), as real data shows this kind of propagation is rear to geological structure, especially for our diverse study area.

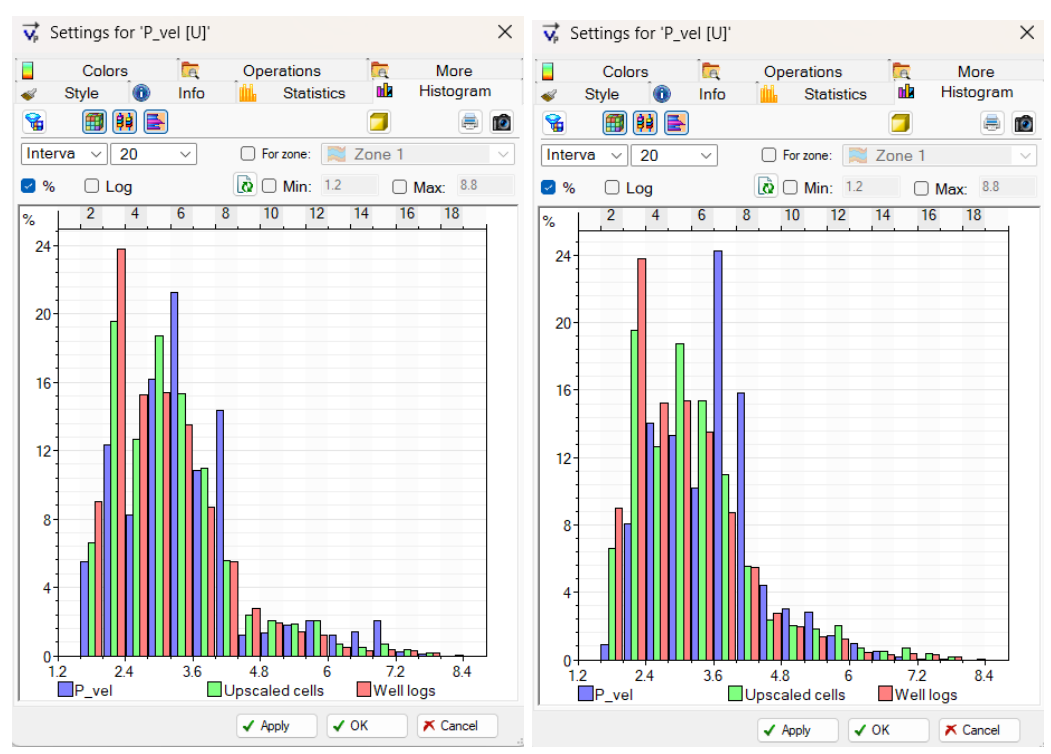


Figure 3.7: Closest (left) and Moving average (right) (Petrel 2013)

Moving Average populates each active cell with a distance-weighted mean of nearby well values found within a 3D boundary. Weight typically follows an inverse-distance law, so closer sample contribute more. The method produces locally smoother field: it preserves broad trends and reduces noise but damps extreme and can blur sharp contrast if the neighborhood is large. This model is fast but it does not model variogram structure or reproduce small-scale heterogeneity. Histogram (Fig. 3.7) shows some similarity with Closest simulation, but show inconsistencies of the histogram compared to well log and scaled data. But 3D model shows a smoother transition compare to Closest method (Fig. 3.8)

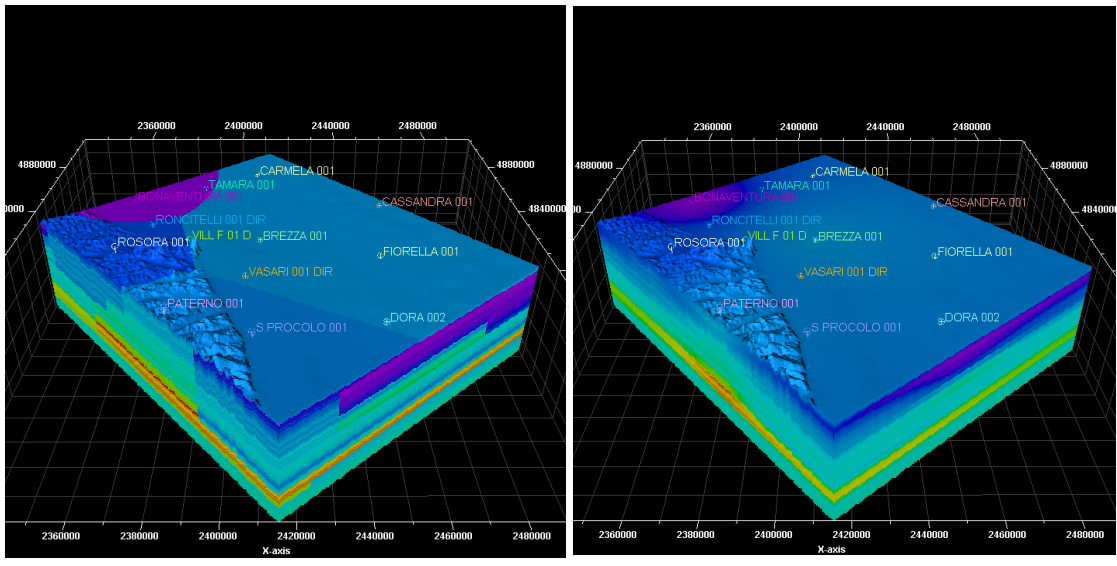


Figure 3.8: 3D model of Closest (left) and Moving average (right) (Petrel 2013)

These four approaches are applied on same zone-facies framework; their outcomes are compared quantitively before selecting the working property models. Closest and Moving average shows big differences in value numbers in histogram (Fig. 3.7) compare to GRFS and SGS histogram (Fig. 3.6), since the well data is the only available for characterizing the study area. Although GRFS and SGS relatively have similar outcome in histograms, but as mentioned before SGS is conditioned to the upscaled well data, so it honors measured values at well location. Whereas GRFS is unconditional and may conflict with observations near wells. Conditioning also improves local geological plausibility while keeping the same large-scale continuity as GRFS. For these reasons, SGS is adopted as the working method.

c. Results

To obtain the results, the following parameters were specified for building the model:

№	Step name	Parameters		
1.	Pillar gridding	I-J increment: 500x500		
		Top boundary: geological surface		
		Bottom boundary: 4000 m below sea level		
2.	Layering	100		
3.	Geometrical	V _p , V _s , Density, Young's moduli		
	modeling			
4.	Scale up well logs	Average method: arithmetic		
		Treat log: as points		
		Method: neighbor		
5.	Petrophysical	Method for zone/facies: Sequential Gaussian simulation		
	modeling	Variogram type: spherical		
		Anisotropy range: 40000 (major dir.), 40000 (minor dir.),		
		100 (vertical)		

Table 3.1: Parameters for 3D model

In Petrel, the 3D property fields are generated by propagating well-derived values across the grid under specific spatial model (Table 3.1), distribution depends on a stochastic parameter that is part of the SGS algorithm. The simulation is path-dependent and seed-controlled: each sample propagation highly dependent on initial value (scaled log data), and visits cells in a randomized sequence. So even with identical input, model obtain different output on repeated runs since the values can be assigned spatially to different cells while the overall statistics remain unchanged. When the initial well data differs in magnitude, even with same facies mix, variogram parameters, depth trends etc., the simulation's trajectory shifts more markedly, and the resulting spatial pattern can be diverged substantially (Fig. 3.9).

An example of a single 3D realization of the V_p property is presented in Fig. 3.10.

In order to evaluate the model uncertainty, the 3D modelling process was run 100 times creating 100 realizations of the V_p property. In this way it was investigated the model uncertainty producing an "average" realization and its standard deviation. In Fig. 3.11 is presented the average V_p property along with its standard deviation. The modeled property shows low velocity values on the uppermost part of the studied region that progressively increase with depth. An interesting feature is that the velocities show low values in the central, central-west part of the model (about 2.5-4.0 km/s) and increase toward the basin edges (5.5-7.5 km/s). Main velocity belt lines up along the long diagonal (north-east to south-west). Gradients are smooth over large area; small, jagged patches around upscaled log points reflect real heterogeneity rather than numerical noise. This distribution matches what typically seen in clastic-carbonate basin setting in the region. Approximately, in 3000 meters depth there are sand cementation and carbonates (limestone) can be observed (north-west face of the cube).

The standard deviation show that the more reliable part of the model are the zones close to the wells while in areas further away from the wells the uncertainty becomes larger due to the low density of the available wells in the study area. (Fig. 3.12)

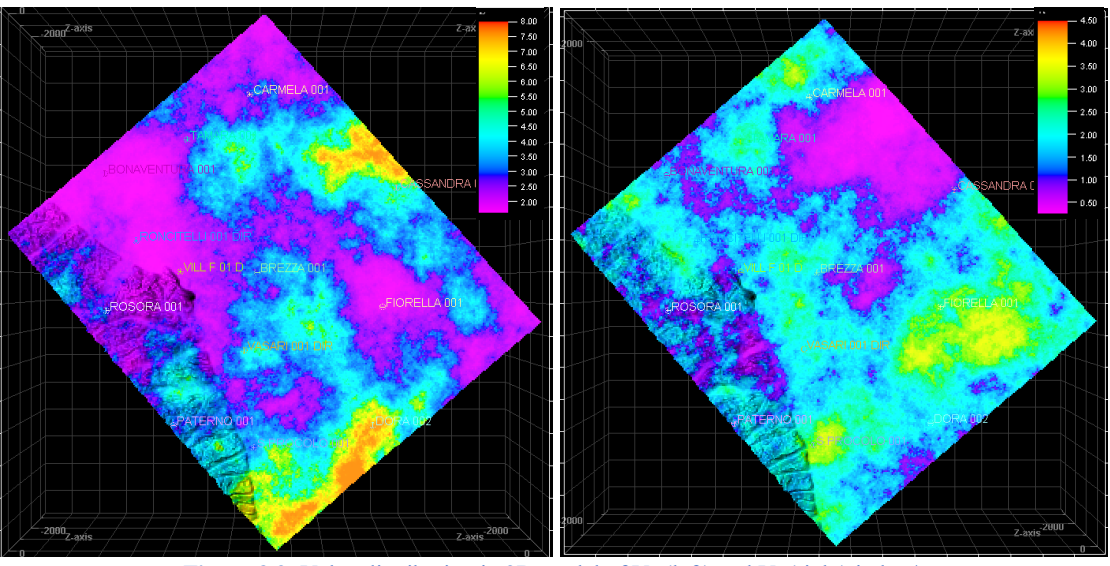


Figure 3.9: Value distribution in 3D model of V_p (left) and V_s (right) in km/s

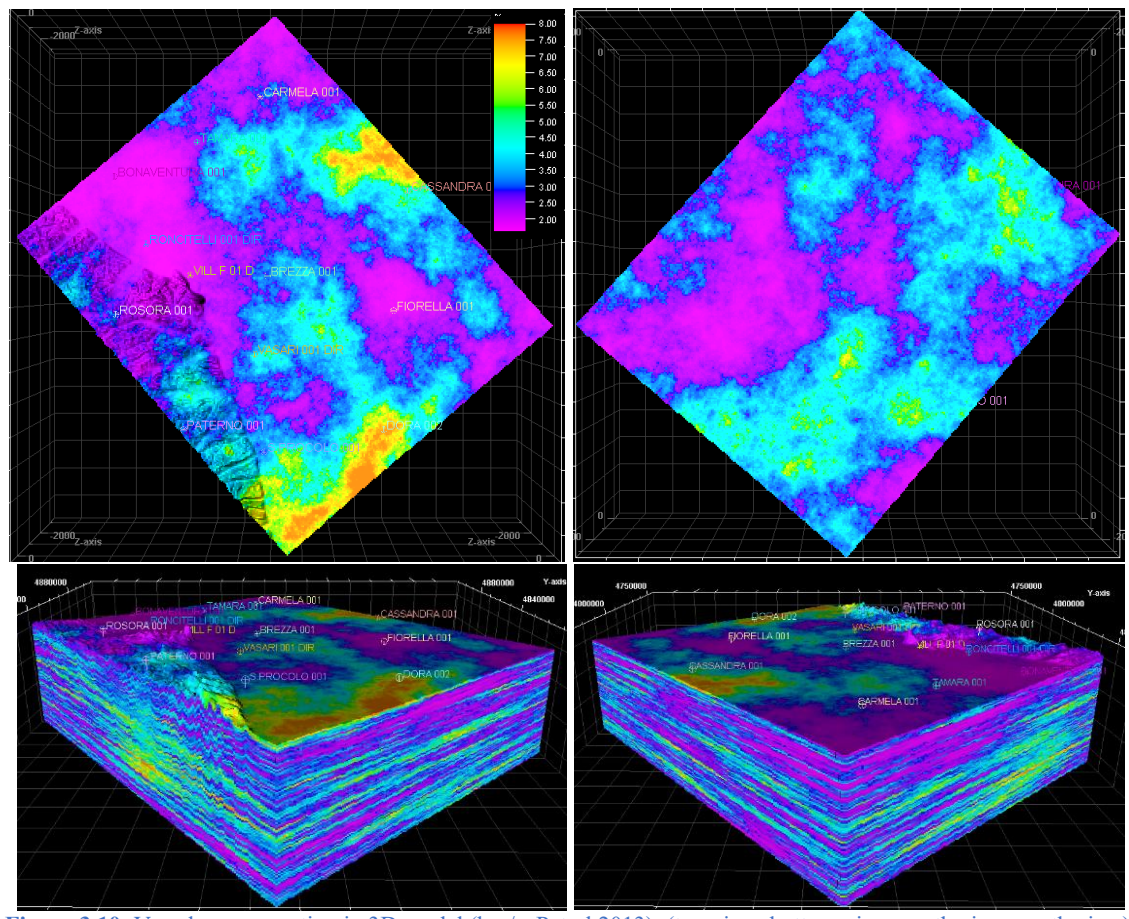


Figure 3.10: V_p value propagation in 3D model (km/s, Petrel 2013). (top view, bottom view, north view, south view)

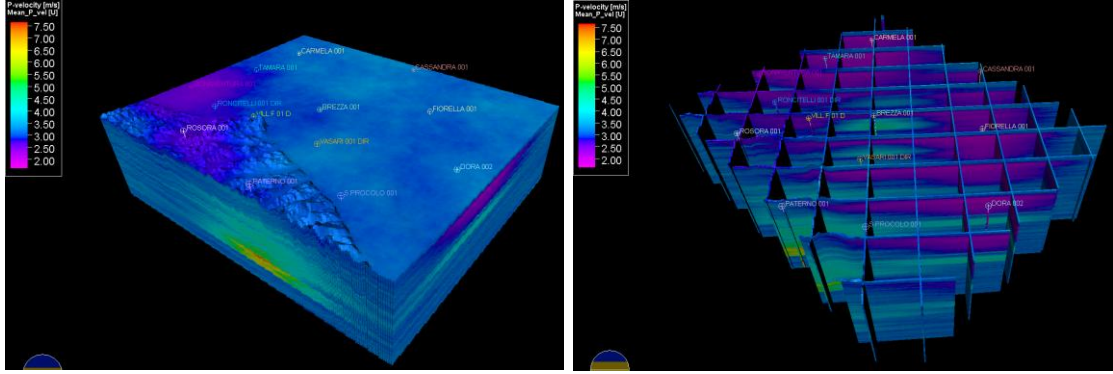


Figure 3.11: 3D model ran 100 times creating 100 realizations of the V_p value (km/s), giving an "average" realization

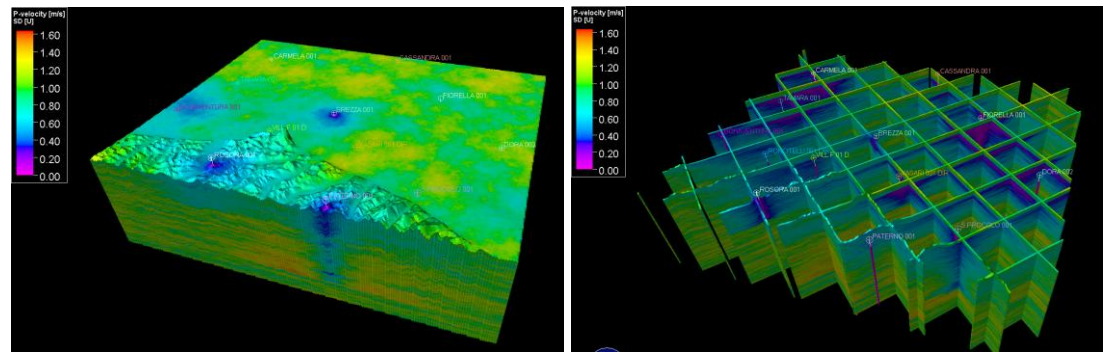


Figure 3.12: Uncertainty in 3D modeling of V_p value

4. CO₂ case study

Carbon capture and storage (CCS) is increasingly gaining importance due to the continuous temperature rising. Emission from heavy industry and power plants remain high even after corrective measures such as the use of renewable power sources; As highlighted by the (IPCC, 2022), credible mitigation pathways therefore integrate CCS alongside renewables and demand-side measures. Market momentum reflects this need: the global CCS project pipeline has expanded rapidly with a capture capacity that has been doubled as under construction facilities start-up (Global CCS Institute, 2024).

According to the most defused cases studies and state-of-the-art reports are presented the parameters for optimal CO₂ storage conditions are presented in Table 4.1.

Porosity threshold of about 20% balances storage capacity and injectivity. At this level pore volume per unit area is large enough to host meaningful CO₂ mass while keeping capillary entry pressure manageable; Moreover, porosity at or above 20% is commonly associated with permeabilities that support field-scale injection rates in siliciclastic reservoirs (Bachu & Adams, 2003). Thicker reservoir increases areal storage efficiency. In multi-layer systems, several thinner units can be substitute for one thick body if they are laterally continuous and connected, but single layers of only a few meters are generally sensitive to local facies variability and well placement (IPCC, 2005). A minimum depth of 800 meters ensures that CO₂ remains supercritical (31.5°C, 73.8 bar) under typical hydrostatic and geothermal gradients. CO₂ in supercritical condition has higher density (improving mass stored per pore volume), lower viscosity, and reduced buoyancy relatively to gaseous condition, all of this enhance storage efficiency and containment margins (IPCC, 2005).

Reservoir properties	Positive indicator	Cautionary indicators
Depth	1000 m ~ 2500 m	less than 800 m or more than 2500m
Reservoir thickness	more than 50 m	Less than 20 m
Porosity	more than 20%	Less than 10%
Stratigraphy	uniform	complex lateral variation
Caprock efficiency		
Lateral continuity	uniform, no faults	lateral variation
Thickness	more than 100 m	less than 20 m

Table 4.1: CO₂ injection criteria (Chadwick, et al., 2008)

Herebelow is presented a short analysis regarding the properties of the rocks encountered in the study area and their capacity of hosting CO₂.

Sandstone usually consisting of clean to moderately shaley sandstones offer acceptable porosity (typically 15-25%) enabling commercial injection rates without excessive pressure buildup.

Sandy clay has lower permeability and higher capillary entry pressure than the underlying sandstone due to fine grains and clay "coatings" reducing throat size. However, sandy clay may appear heterogeneous and could have sand streaks, so it is best treated as a

"baffle" seal. It slows vertical leakage and increase residence time, enhancing dissolution trapping, but cannot relied as the only barrier.

Clay-rich mudrock provide as the main hydraulic seal due to low permeability, high entry pressure, ductile behavior provides a robust hydraulic seal and pressure containment. Their very low vertical connectivity prevents upward mitigation.

Although carbonates could have high porosity, their permeability often dominates by vugs, fractures, and they often lie deep into the earth crust which makes injection economically not profitable.

Most parameters listed in Table 4.1 are directly retrievable from available data and modeling workflow. The only quantity not measured in the dataset is porosity (ϕ) . Because no direct porosity logs or core measurement are available, porosity will be inferred empirically from elastic and density properties computed in this study – namely V_p , V_s , density, and dynamic Young's modulus – using facies specific transforms.

To justify the link between the studied properties (V_p , V_s , density, dynamic Young's modulus) with porosity, we introduce Unconfined Compressive Strength (UCS) as the intermediate variable. UCS is the peak axial stress an intact rock specimen sustains without lateral confinement (Mavko, et al., 2009); it is a first-order measure of rock competence that responds to grain framework, cementation, microcrack and pore structure. Empirically, UCS correlates positively with dynamic stiffness measures (E, V_s) and negatively with porosity and clay content. Among the available pathways, we adopt the $E \to UCS \to \phi$, because E already encapsulates the information carried by V_p , V_s , density into a single, physically meaningful stiffness metric.

Empirical relations for sandstones (Mavko, et al., 2009).

Unconfined compressive strength derives from Young's modulus (Bradford, et al., 1998):

$$UCS = 2.28 + 4.1089 \times E \quad [MPa]$$
 (10)

Young's modulus (E) defined in GPa

Porosity – UCS relation will use empirical formula as below (Vernik, et al., 1993):

$$UCS = 254 \times (1 - 2.7 \times \varphi)^2 \quad [MPa]$$
 (11)

Using equation (10) and (11), we will derive the relation between φ and E:

$$UCS = 2.28 + 4.1089 \times E = 254 \times (1 - 2.7 \times \varphi)^{2}$$
$$\frac{2.28 + 4.1089 \times E}{254} = (1 - 2.7 \times \varphi)^{2}$$
$$\sqrt{\frac{2.28 + 4.1089 \times E}{254}} = 1 - 2.7 \times \varphi$$

$$\varphi = \frac{1 - \sqrt{\frac{2.28 + 4.1089 \times E}{254}}}{2.7} \tag{12}$$

We will also apply a claystone-specific empirical porosity relation to verify its sealing capacity and confirm that porosity remain sufficiently low for effective caprock performance.

Unconfined compressive strength - Young's modulus (Chang, et al., 2004):

$$UCS = 7.22 \times E^{0.712} \quad [MPa] \tag{13}$$

Young's modulus (E) defined in GPa

Porosity – UCS relation will use empirical formula as below (Horsrud, 2001):

$$UCS = 2.922 \times \varphi^{-0.96} \quad [MPa]$$
 (14)

Using equation (13) and (14), we will derive the relation between φ and E for claystone:

$$UCS = 7.22 \times E^{0.712} = 2.922 \times \varphi^{-0.96}$$

$$\varphi^{-0.96} = \frac{7.22 \times E^{0.712}}{2.922}$$

$$\varphi = (\frac{7.22 \times E^{0.712}}{2.922})^{-1.0416}$$
(15)

Only 8 out of 13 wells intersect a sandstone interval; remaining wells either did not encounter sandstone or do not show a sandstone signature in their logs (Table 4.2)

Well name	Intersected layers (TVDSS, m)		
	Claystone	Sandy clay	Sandstone
VILLA FELICI 001 DIR	381 ~ 486	-	489 ~ 516
	519 ~ 812	816 ~ 1280	-
	$1282 \sim 1320$	1322 ~ 1412	1416~1624
VASARI 001 DIR	353 ~ 782	785 ~ 875	877 ~ 945
	-	949 ~ 970	973 ~ 1080
	-	1087 ~ 1128	-
PATERNO 001	130 ~ 491	495 ~ 1154	1158 ~ 2155
	=	$2160 \sim 2288$	2291 ~ 2379
S. PROCOLO 001	309 ~ 909	913 ~ 1471	1477 ~ 1609
	-	1611 ~ 1773	1774 ~ 1845
	=	1848 ~ 2505	2510 ~ 2599
DORA 002	-	$307 \sim 887$	893 ~ 938
	=	940 ~ 1100	1103 ~ 1383
BREZZA 001	=	100 ~ 137	139 ~ 168
	-	171 ~ 446	448 ~ 600
	-	603 ~ 667	-
BONAVENTURA 001	103 ~ 545	550 ~ 988	991 ~ 2426
TAMARA 001	349 ~ 1524	1526 ~ 2164	2168 ~ 2358
	-	2361 ~3400	-

Table 4.2: Well intersection with lithology

"VILLA FELICI 001 DIR" crosses sandstone in two intervals $-489\sim516$ m and $1416\sim1624$ m (TVDSS). Applying the ≥800 meters depth criterion for supercritical CO₂

the shallow interval is discarded and only 1416~1624 m is retained. "BREZZA 001" does not contain sandstone bellow 800 m and is therefore excluded from the candidate set. "TAMARA 001" encounters sandstone too deep for consideration, at ~2168 m TVDSS.

Retained sandstone intervals and wells were then used as input to the empirical E-porosity relation. Claystone porosity also computed to ensure caprock efficiency. The resulting porosity estimates are reported and will be visualized on a depth-porosity diagram (Fig. 4.1). Figure provides a direct view of how porosity evolves with depth.

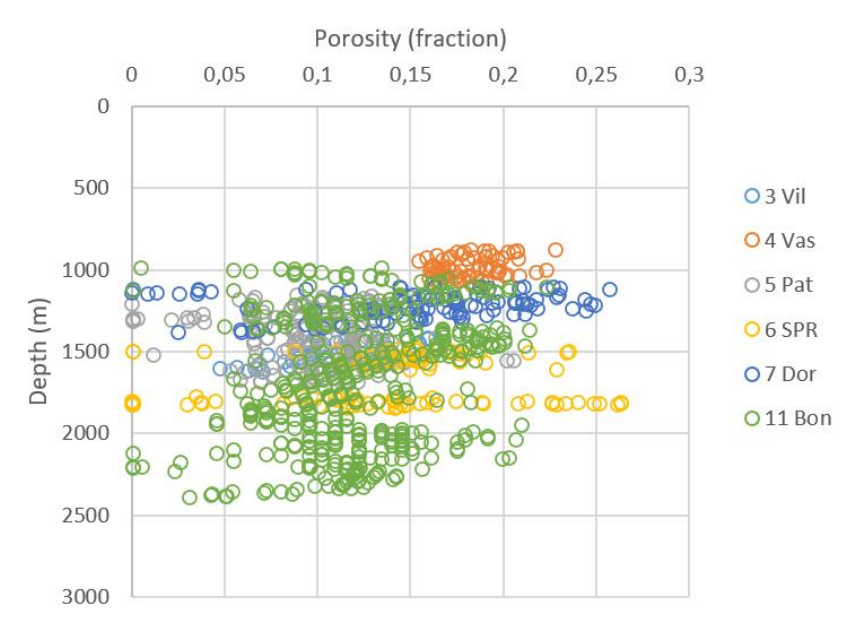


Figure 4.1: Porosity-depth cross plot in sandstone section (numeration of well refers to Table 2.1)

The sandstone results display a broad spread: φ commonly ranges from 0.05 to 0.25, with no clear clustering by depth or porosity. Apart from "VASARI 001 DIR" well, which forms relatively tight band around 0.15~0.20, whereas the other wells show strong heterogeneity. This dispersion is consistent with variable grain size and sorting, patchy cementation, and localized diagenetic overprint; it may also reflect the mixed stress state and facies transition captured in E.

The selected "VASARI 001 DIR" well encounters, from top to base, claystone → sandy clay → sandstone → claystone (Fig. 4.2). Consistent with the storage concept adopted here, the claystone unit is taken as the primary caprock. Within the reservoir section, the sandstone is locally interrupted by a sandy clay interbed at 949-970 m TVDSS, which divides the sandstone into two sub-intervals. For volumetric screening, these flanking sandstone segments are treated as single reservoir body with the 949-970 m sandy clay slice excluded from reservoir thickness. This treatment preserves the effective net to gross (NTG) of the sandstone while acknowledging the presence of thin, lower-permeability layer that may compartmentalize short-range flow but does not compromise the overall reservoir-seal architecture.

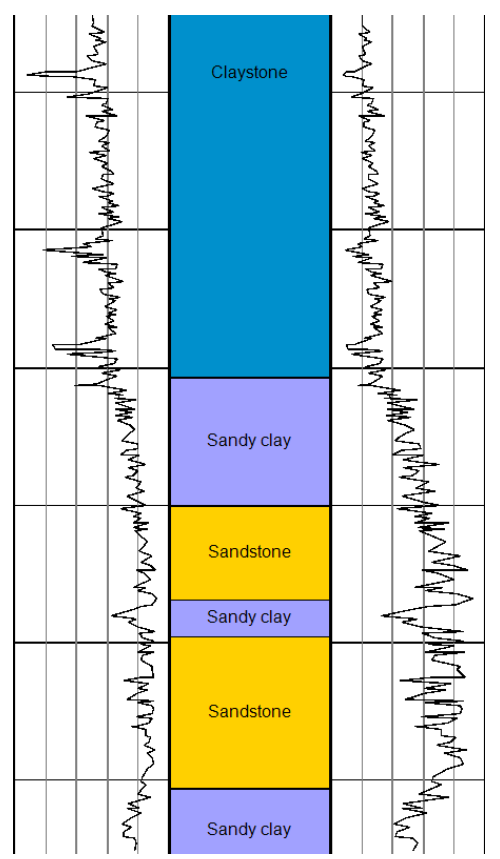


Figure 4.2: VASARI 001 DIR well section (DT, lithology, Young's modulus)

After computing porosity (ϕ) from the empirical $E \to \phi$, we derive an average porosity for the sandstone reservoir interval using a thickness-weighted aggregation, each data contributes in proportion to its interested thickness along the well path. The averaging formula is given by:

$$\varphi_{av} = \frac{\sum \varphi_i h_i}{\sum h_i}$$

φ_i – porosity at given depth;

h_i- intersected thickness of porosity;

After computing porosity and determining net thickness, we obtain the following parameters (Table 4.3):

Layers	Thicknes	s (m)	Average porosity	
Sandstone 1	69,986662	190 6702701	0,186509594	0.192004625
Sandstone 2	110,6837081	180,6703701	0,180625159	0,182904625

Table 4.3: Thickness and average porosity of sandstone (VASARI 001 DIR)

To estimate the lateral extent of the sandstone, we first examine the well data. Wells "VILLA FELICI 001 DIR", "PATERNO 001", "S. PROCOLO 001", "DORA 002" and "BREZZA 001" are distributed around "VASARI 001 DIR" (Fig. 4.3), which we consider at the center of the reservoir interpretation. All of the surrounding well also encounter sandstone layers (Table 4.2), but at different depth, indicating structural relief and/or stratigraphic discontinuities rather than a single, perfectly flat sheet. Only well "DORA 002" intersects sandstone at comparable depth to our main well, although its section is

interrupted by thicker sandy clay interbed. This correlation characteristics supports the working hypothesis that reservoir body is slightly elongated toward well "DORA 002".

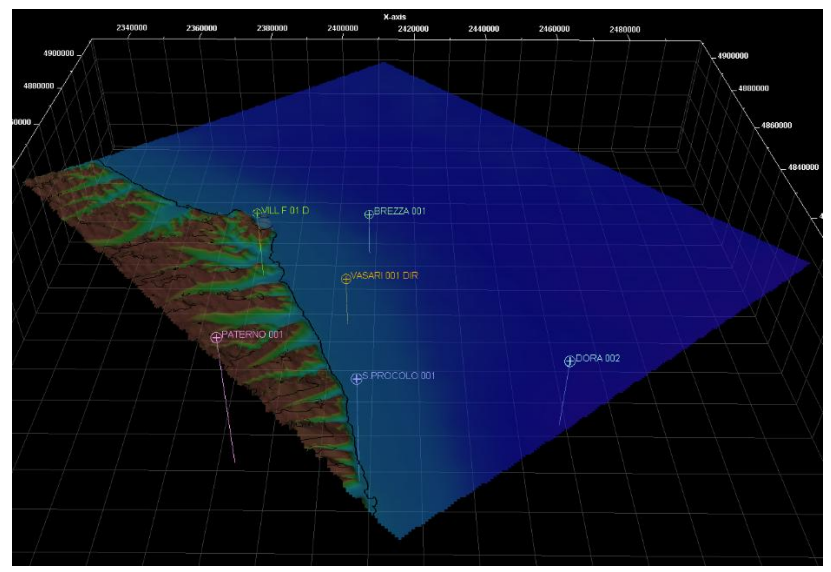


Figure 4.3: Well cluster around VASARI 001 DIR well

Given this observation and the sparse spacing of control, the areal footprint will be evaluated under three scenarios (Fig. 4.4): (i) an optimistic case that spans the full available area almost approaching to "DORA 002"; (ii) most likely case constrained by consistent depth reaching mid distance between "VASARI 001 DIR" and "DORA 002"; (iii) a conservative case restricted to the nearest are of "VASARI 001 DIR". Each scenario will be using same volumetric shape to calculate the range of possible reservoir volume. Shape will be assumed as ellipsoid, so the area calculated by using:

$$A = \pi \times a \times b$$

where a and b are semi major and semi minor axes.

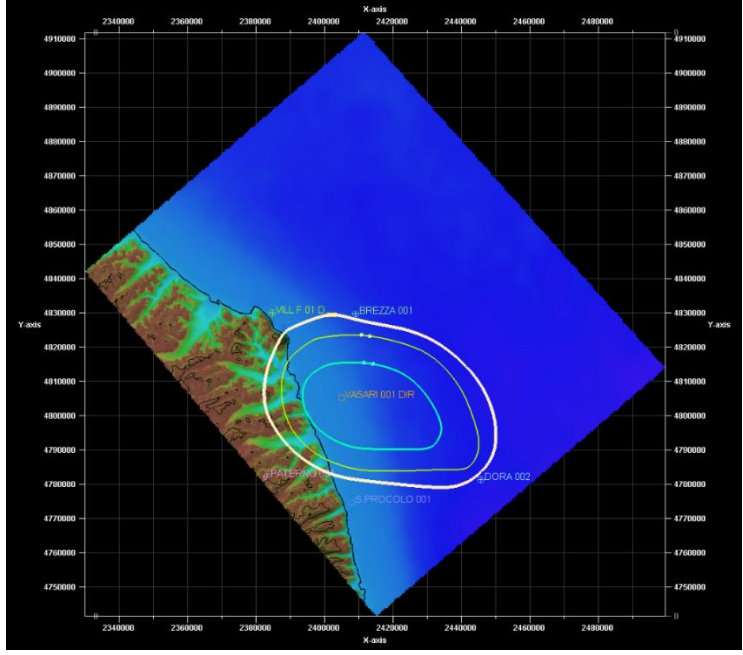


Figure 4.4: Three scenarios for area of regional aquifer

Because there is no evidence in the available records to demonstrate that this body is a depleted hydrocarbon reservoir, it will be treated here as a saline aquifer. For estimating the reservoir's CO₂ storage potential, also known as effective storage capacity (Bachu, et al., 2007):

$$M_{CO_2} = A \times h \times \varphi \times \rho_{CO_2(r)} \times S_{eff} \text{ [kg]}$$
 (16)

A – area of regional aquifer;

h – average thickness of regional aquifer;

 ϕ – average reservoir porosity of the aquifer;

 $\rho_{CO_2(r)}$ – CO₂ density at reservoir conditions;

 S_{eff} – storage efficiency factor;

Under hydrostatic conditions and geothermal gradient of 25 °C/km from a 15 °C surface temperature (using data from Angus (Angus, et al., 1973)), the density of CO₂ increase sharply near ~800 m, coincident with the transition to the supercritical region (Fig. 4.5). Above this depth the fluid is gas-like and occupies a much larger specific volume (illustrated by the cubes), so the apparent volume collapses rapidly with depth as pressure and temperature rises. Beyond 1.5 km, both density and specific volume approach a nearplateau, indicating that further depth change almost negligible. Below 800 m level CO₂ attains high density and relatively low compressibility and viscosity, which together improve storage efficiency and injectivity while moderating buoyancy (Benson & Cook, 2008). In our case injection depth is 870-1080 m, which gives us approximately 570 kg/m³.

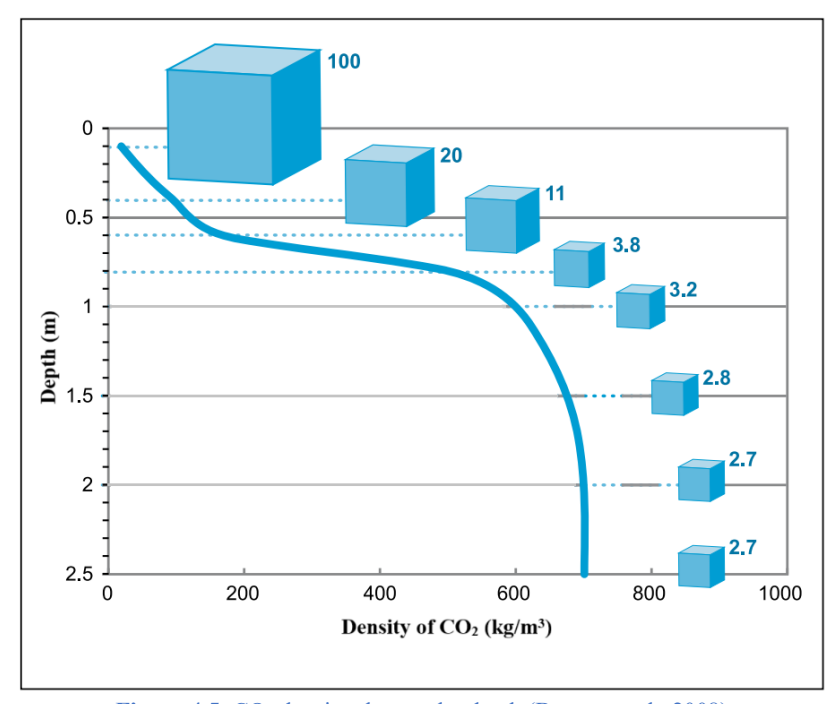


Figure 4.5: CO₂ density changes by depth (Benson et al., 2008)

S_{eff} represents the fraction of the gross pore volume that can be actually occupied by injection of CO₂ under realistic constrains, like limited sweep because of mobility contrast and gravity override, incomplete is contact, heterogeneity, capillary entry effect, well spacing and other parameters that affects to CO₂ injectivity. In regional screening of saline aquifers, these effects collectively reduce usable pore volume to only few percent. Following Frailey's (Frailey, et al., 2020) Illinois basin application methodology, we adopt a saline-aquifer storage efficiency factor S_{eff} in the range 1-4% for prospective capacity (Frailey, et al., 2020). In the study to see all outcome we will carry the full range through the calculation and report results, rather than a single point estimate (Table 4.4).

Parameters for №16 formula						
Thickness	Average	CO ₂ density	Area of	Storage	Effective	
(m)	porosity	at reservoir	regional	efficiency	storage	
	(φ,	conditions	aquifer	factor	capacity	
	fraction)	$(\rho_{CO_2(r)},$	$(A, 10^6 \mathrm{m}^2)$	$(S_{\rm eff}, \%)$	$(M_{CO_2}, 10^6)$	
		kg/m^3			tons)	
180,67	0,183	570	2627	1	495	
				2	990	
				3	1485	
				4	1980	
				1	345	
			1831	2	690	
				3	1035	
				4	1380	
			844	1	159	
				2	318	
				3	477	
				4	636	

Table 4.4: Final results of effective storage capacity

Conclusion

This thesis followed a well-known workflow using publicly available information for a preliminary assessment of CO₂ storage in central Italy. It began with a reduced set of wells derived from public sources: 13 candidates were retained to balance data quality and coverage across the Marche–Ancona region and the adjacent Adriatic shelf. An important part of the thesis was the digitalization of DT-Sonic well logs derived from 1:1000 geological profiles. The work included scanning, digitization, removal of nonformation interval (casing/cement near surface), and consistent quality checks along depth. With digitalized DT there were assembled facies-specific empirical relations to derive V_p, V_s, bulk density, and dynamic Young's modulus (E), and performed data validation using cross-plots.

The constructed logs were loaded into Schlumberger Petrel (v.2013.1). It was generated a simplified 3D geocellular model. Inside this model were upscaled the available logs and the V_p property was distributed in 3D using a set of different distribution methods (Gaussian random, sequential Gaussian, moving average, and closest as a diagnostic contrast). Sequential Gaussian simulation was adopted as the preferred algorithm because it honors well information and yields an uncertainty envelope rather than a single smoothed field. Then a statistical analysis was made in order to evaluate an average V_p distribution with its corresponding standard deviation. The results of the geological modelling provided insights into lateral and vertical sonic-velocity variations with depth for the central-eastern part of Italy.

The last part of the thesis is dedicated to a preliminary calculation of a sandy layer as a candidate for a future CO_2 storage site. Porosity was one of the missing parameters for the storage capacity calculation. Since no direct porosity data were available to compute effective storage capacity, the property was estimated through a workflow ($E \rightarrow UCS \rightarrow \phi$), leveraging the fact that E already encapsulates information from V_p , V_s , and bulk density. The resulting sandstone porosities span roughly the rage 0.05--0.25, with a local clustering in one of the available wells. After volumetric calculations based on published formulas, the estimated storage capacity ranges between $159\text{--}1980 \times 10^6$ tons of CO_2 , depending on S_{eff} and the extent of the regional aquifer.

The resolution of the final 3D model and of the storage capacity are strongly connected to the density of available wells (13 wells across a wide region). The geological model, from the structural and stratigraphic point of view, also carries uncertainties due to insufficient fault characterization, as precise fault geometry was not available. For that reason, the lowest end of the storage capacity calculation seems more plausible. Nevertheless, the preliminary estimation of the storage capacity of a sandy layer identified in the area showed that the Adriatic offshore and Ancona sector are promising for CCS: the area is characterized by caprock-reservoir systems of sandstone, sandy clay, and claystone; depth interval in most cases already satisfying supercritical conditions; and the region's petroleum legacy suggesting practical pathways for subsurface operations.

References

- Amorosi, A., Maselli, V. & Trincardi, F., 2015. Onshore to offshore anatomy of a late Quaternary source-to-sink system (Po Plain–Adriatic Sea, Italy). *Earth-Science Reviews*.
- Angus, S., Armstrong, B. & Reuck, K. d., 1973. *International Thermodynamic Tables of the Fluid State Volume 3. Carbon Dioxide*. London, UK: Pergamon Press.
- Bachu, S. & Adams, J., 2003. Sequestration of CO2 in Geological Media in Response to Climate Change: Capacity of Deep Saline Aquifer to Sequester CO2 in Solution.. *Energy Conversion and Management*.
- Bachu, S. et al., 2007. CO2 storage capacity estimation: Methodology and gaps,. *International Journal of Greenhouse Gas Control*.
- Benson, S. & Cook, P., 2008. Underground geological storage,. *IPCC Special Report on Carbon dioxide Capture and Storage*..
- Bradford, I. D. R., Fuller, J., Thompson, P. & and Walsgrove, T., 1998. Benefits of assessing the solids production risk in a North Sea reservoir using elastoplastic modeling: SPE/ISRM 47360, SPE/ISRM. *Eurock* '98...
- Castagna, J., Batzle, M. & Kan, T., 1993. Rock physics-The link between rock properties and AVO response.. *Rock Physics*.
- Castagna, J. P., Batzle, M. L. & Eastwood, R. L., 1985. Relationships between compressional-wave and shear-wave velocities in elastic silicate rocks. *Geophysics*.
- Chadwick, A. et al., 2008. BEST PRACTICE FOR THE STORAGE OF CO2 IN SALINE AQUIFERS. Nottingham, UK.: British Geological Survey.
- Chang, C., Zoback, M. & Khaksar, A., 2004. Rock strength and physical property measurements in sedimentary rocks,. *SRB Annual Report*..
- Conti, P., Cornamusini, G. & Carmignani, L., 2020. An outline of the geology of the Northern Apennines (Italy), with Geological Map at 1:250,000 scale. *Italian Journal of Geosciences*.
- Cota, L. & Baric, G., 1998. Petroleum potential of the Adriatic offshore, Croatia. *Organic Geochemistry*.
- Fantoni, R. & Franciosi, R., 2010. Tectono-sedimentary setting of the Po Plain and Adriatic Foreland. *Rendiconti Lincei. Scienze Fisiche e Naturali*.
- Fjaer, E., Holt, R. M., Raaen, A. & Risnes, R., 2008. *Petroleum Related Rock Mechanics*. *2nd edition*. s.l.:s.n.
- Frailey, S., Koperna, G. & Tucker, O., 2020. The CO2 Storage Resource Management System (SRMS): A Project Maturity Based Classification and Categorization of Storable Quantities. s.l., s.n.

Gardner, G., Gardner, L. & Gregory, A., 1974. Formation Velocity and Density—The Diagnostic Basics for Stratigraphic Traps. *Geophysics*.

Global CCS Institute, 2024. *Global satatus of CCS 2024: Collaborating for a net-zero future*. s.l., Global CCS Institute.

Han, D., Nur, A. & D., M., 1986. Effects of Porosity and Clay Content on Wave Velocities in Sandstones. *Geophysics*.

Horsrud, P., 2001. Estimating mechanical properties of shale from empirical correlations. *SPE Drilling Completion*.

IPCC, 2005. Carbon dioxide capture and storage. Cambridge, UK: Cambridge university press.

IPCC, 2022. Climate Change 2022: Impacts, Adaptation and Vulnerability. Cambridge, UK, Cambridge University Press..

Maselli, V. et al., 2011. High-frequency sea level and sediment supply fluctuations during Termination I: An integrated sequence-stratigraphy and modeling approach from the Adriatic Sea (Central Mediterranean). *Marine Geology*.

Mavko, G., Mukerji, T. & Dvorkin, J., 2009. *The Rock Physics Handbook, 2nd Edition*.. New York: Cambridge University Press.

Morteza, S., P., V. & Vasarhelyi, B., 2020. Investigation of the relationship between dynamic and static deformation moduli of rocks. *Geomech. Geophys. Geo-energ. Geo-resour.*

Nasim, M. Q. et al., 2023. VeerNet: Using Deep Neural Networks for Curve Classification and Digitization of Raster Well-Log Images. *Journal of imagining*.

Oluić, M., Morović, M. & Ivanov, A., 2020. Detection of Oil Slicks in the Adriatic Sea (Mediterranean) Using Satellite SAR Imagery. *Athens Journal of Technology and Engineering*.

Pickett, G., 1963. Acoustic character logs and their applications in formation evaluation. *J. Petrol. Technol.*.

Picotti, V. et al., 2007. The Miocene Petroleum System of the Northern Apennines in the Central Po Plain (Italy). *Frontiers in Earth Sciences*.

Teloni, S. et al., 2024. Morphostructural evidence of crustal-scale, active along-strike segmentation of the Umbria-Marche Apennines, Italy. *Tectonophysics*.

Vernik, L., Bruno, M. & Bovberg, C., 1993. Empirical relations between compressive strength and porosity of siliciclastic rocks. *Int. J. Rock Mech. Min. Sci. Geomech. Abstracts.*.